FINITE ELEMENT ANALYSIS OF THE MESOSPHERE'S ELECTROMAGNETIC

RESPONSE TO LARGE SCALE LIGHTNING ASSOCIATED WITH

SPRITES AND OTHER TRANSIENT LUMINOUS EVENTS

Except where reference is made to the work of others, the work described in this thesis is my own or was done in collaboration with my advisory committee. This thesis does not include proprietary or classified information.

_____

Michael David Allgood

Certificate of Approval:

_____	_____
Lloyd S. Riggs	Michael E. Baginski, Chair
Professor	Associate Professor
Electrical and Computer Engineering	Electrical and Computer Engineering
_____	_____
Stuart M. Wentworth	Joe F. Pittman
Associate Professor	Interim Dean
Electrical and Computer Engineering	Graduate School

FINITE ELEMENT ANALYSIS OF THE MESOSPHERE'S ELECTROMAGNETIC RESPONSE TO LARGE SCALE LIGHTNING ASSOCIATED WITH SPRITES AND OTHER TRANSIENT LUMINOUS EVENTS

Michael David Allgood

A Thesis

Submitted to

the Graduate Faculty of

Auburn University

in Partial Fulfillment of the

Requirements for the

Degree of

Master of Science

Auburn, Alabama
May 10, 2008

FINITE ELEMENT ANALYSIS OF THE MESOSPHERE'S ELECTROMAGNETIC RESPONSE TO LARGE SCALE LIGHTNING ASSOCIATED WITH SPRITES AND OTHER TRANSIENT LUMINOUS EVENTS

Michael David Allgood

_____
Signature of Author

_____
Date of Graduation

THESIS ABSTRACT

FINITE ELEMENT ANALYSIS OF THE MESOSPHERE'S ELECTROMAGNETIC RESPONSE TO LARGE SCALE LIGHTNING ASSOCIATED WITH SPRITES AND OTHER TRANSIENT LUMINOUS EVENTS

Michael Allgood

Master of Science, May 10, 2008
(B.E.E., Auburn University, 2001)

82 Typed Pages

Directed by Michael E. Baginski

In this research, a numerical investigation of high altitude sprites and other mesospheric Transient Luminous Events induced by lightning is presented. A Finite Element Model is created using equations based on a modified form of Maxwell's equations and includes the effects of ionization on the upper atmosphere. Results will first be shown for standard models with constant ambient conductivity which will be verified based on prior research. A model will then be introduced which includes ionization effects altering the electron conductivity in a non-linear manner. These results will be compared to previously published research.

ACKNOWLEDGEMENTS

The author would like to express his appreciation to Dr. Michael Baginski for the many years of advice and patience shown to me throughout this entire process. He would also like to thank both Dr. Lloyd Riggs and Dr. Stuart Wentworth for their friendship and assistance. He would like to acknowledge the Department of Defense for the reception of a National Defense Science and Engineering Fellowship without which this work never would have started. His company, Dynetics Inc., provided financial support through the last few years. The Alabama Supercomputing Authority provided the necessary hardware and software for completion of this research. He would also like to recognize Dr. V. P. Pasko for providing data and a figure from his previous work. Finally, special thanks go to his wife, Sydney, without whose support, patience, and motivation, this research would have ended many years ago.

Style manual or journal used IEEE Transactions on Microwave Theory and Techniques.

Computer software used Microsoft Word 2003 and 2007.

TABLE OF CONTENTS

LIST OF FIGURES

CHAPTER 1

INTRODUCTION

On a night in July of 1989, two frames of video captured flashes of light discharging between the top of clouds and the ionosphere [1]. Before this night, there were scattered reports of mysterious lights high above thunderclouds. For years pilots would also occasionally observe luminous events above storms [1]. Without video evidence, however, only a handful of researchers gave a second thought to this unusual occurrence. After that fateful night, more observations were documented leading to a surge of investigators trying to determine the underlying cause and properties of this phenomenon, known as a sprite.

1.1 Characteristics of Sprites

A sprite is an electrical phenomenon occurring above the thunderclouds in the upper atmosphere immediately following an intense lightning discharge. This phenomenon appears as an optical flash which has been reported at altitudes ranging from ~ 60 km up to ~ 95 km, in the region known as the mesosphere [2-6]. Sprites are usually caused by a positive Cloud-to-Ground (CG) stroke [7, 8] while some sprite observations have been linked to negative CG strokes also [9]. These CG strokes create large quasi-electrostatic (QE) fields which produce the sprites [10]. Sprites tend to be red in color near its top due to nitrogen ionization (first positive emission) [7] and blue in color near its bottom due to nitrogen ionization (first negative emission) [7]. Simulations

have indicated that the conditions allowing sprite development occur only at night [11].

The spatial structure of a sprite event can have vertical extents of up to 30 km with lateral extents of up to 100 km in diameter [12-14]. While sprites typically occur in a large region of the upper atmosphere, it has been shown that it is in a narrow area from 70-75 km where they initiate [15, 16]. This has been confirmed by models indicating large electric fields develop at these altitudes [15]. Within this region, the sprites are composed of filamentary columns, numbering up to 20, each with a diameter of 0.5-5 km [14, 17, 18]. They travel downwards from the upper atmosphere to the thunderclouds at velocities up to over 10^7 m/s [19]. There is a slight temporal delay after the CG lightning discharge of up to 200 ms until the sprite becomes visible [14, 20].

1.2 Additional Transient Luminous Events

Sprites are not the only atmospheric phenomenon which has optical emissions in the upper atmosphere. Another type of Transient Luminous Event (TLE) are known as elves, normally described as disk-like [17, 21]. These appear at altitudes ranging from ~ 75-105 km with lateral extents from 200-660 km [9, 17, 21]. The elves are believed to be produced by the heating of ambient electrons due to EMP fields [9, 14, 17]. These TLEs tend to start ~ 100-200 μs after the lightning discharge and only last approximately ~ 1 ms [9, 21].

A third distinct type of TLE are blue jets which are described as "blue conical shapes" [13]. As opposed to the sprites, these events propagate upwards from the thunderclouds at lower velocities [13, 22]. The lateral extents of the blue jets appear to range from 35-40 km [22, 23]. Gigantic jets have also been discovered which reach altitudes of ~ 90 km with diameters of ~ 40 km [22].

The most recent type of TLE discovered are known as sprite halos, originally mistaken for elves. These appear to be produced by QE fields, not EMP fields which are related to the creation of elves [14]. The sprite halo occurs before the formation of the sprites and is seen as a glow at the sprites' vertical extent [14]. Halos can have lateral extents of less than 100 km in diameter and only have a duration of ~ 1 ms [24, 25].

1.3 Sprite Observations

For over a century, reports have circulated of these lighting discharges originating from the clouds and traveling upwards [1]. It has only been in the past couple of decades however that recorded images have appeared. A brief summary of these observations follows.

1.3.1 First Recorded Image

The first images of an electrical discharge flowing upwards from thunderstorm cloud tops were recorded in Minnesota using a "low-light-level TV camera" the night of July 5, 1989 [1]. Over two frames of film, a team observed twin flashes of light initiated in cloud tops and dissipating in the upper atmosphere [1]. The flashes were calculated to have a vertical extent of ~ 20 km with a separation of ~ 4 km [1]. The light was also calculated to be 50 to 100 times as intense as the CG discharges recorded around the same time [1].

1.3.2 Space Shuttle Images

In an effort to collect data concerning lightning events, cameras mounted on the space shuttle's payload bay where used in a project called the Mesoscale Lightning Experiment (MLE) [26-29]. After the first mission, control of the cameras was given to a ground crew allowing for around the clock operation [26]. During the time period from

1989 through 1991, video from this experiment has identified 17 separate occurrences of TLEs [27-29]. Based on the number of CG events recorded over the same period, it is estimated that 1 out of every 5000 of CG discharges results in a sprite [27, 28]. In addition to the sprite events, one instance of a blue jet and elve were also recorded [29].

1.3.3 Images Recorded from Aircraft

There have been multiple attempts to capture TLEs using cameras mounted aboard aircraft flying above thunderstorms. In July 1993, 19 events were captured over the Midwest United States aboard a NASA owned DC-8 [2]. The duration of these events was estimated to be approximately 16 ms with an occurrence rate of 1 out of every 200-300 CG discharges [2]. Over a two week period during the summer of 1994, observations of upper atmospheric TLEs were conducted in the Sprites94 aircraft campaign [2]. During this campaign, approximately 500 sprite events and 56 blue jets were recorded [2]. The sprites appeared both alone and in clusters of two or more, with clusters being more prevalent [2].

1.3.4 Further Ground-Based Recordings

Since the first recorded images of sprites in 1989, thousands of sprites and other TLEs have been observed during numerous campaigns. In October of 1997, high speed recordings captured 42 sprite clusters, along with 4 sprite halos which have a temporal resolution on the order of ~ 1 ms [30]. On August 29, 1998, two sprites were detected in Mexico resulting from negative CG discharges [31]. A campaign during the early summer of 2000 called STEPS, centered at Goodland, KS, recorded 1237 TLEs with approximately 90% being sprites [32].

1.4 Overview and Historical Perspective

Along with all the visual evidence of Sprites, there have been numerous attempts to theoretically predict and describe these events. The earliest paper that suggests the possibility of sprites occurring was published in 1925 by C. T. R. Wilson [33]. Wilson mentions what he calls both a "critical value" and a "sparkling limit." When the electric field at some altitude above the thundercloud exceeds this value, ionization occurs, resulting in the possibility of an electrical discharge [33]. Wilson assumes "the critical field to remain proportional to the pressure" [33] which in turn allows a small electric field at higher altitudes to result in a discharge.

1.4.1 Measurements in the Middle Atmosphere and Ionosphere

Measurements presented in a 1984 paper by Hale [34] showed some of the peculiarities of the electric field's behavior in the middle to upper atmosphere which could be associated to Sprites. The measurements showed the relaxation time at higher altitudes to be comparable to that at the source of the lightning perturbation [34]. This differed from the theories at the time which predicted local relaxation times several orders of magnitude shorter. Hale also suggests that the energy dissipated in this region is nearly equivalent to that of the lightning stroke [34].

1.4.2 Finite Element Model using Ambient Conductivity Profiles

Baginski [35] used a finite element model to predict the resulting electric fields in the upper atmosphere due to charge perturbations associated with lightning. His model solved the complete set of Maxwell's Equations. Baginski uses three different conductivity profiles which include the Gish model, an exponential model, and a model based on measured data.

The results from Baginski's model confirm Hale's observations of longer temporal duration in the middle and upper atmosphere [35]. The electric fields show a sharp drop after the initial peak, followed by a slow, steady decay in the late-time region. He concludes that it is this late-time duration which increases the amount of energy dissipated in the region [35].

1.4.3 Non-Linear Conductivity Profile

An iterative approach using a conductivity profile developed by Pasko [36, 37] was introduced which explained the break-down of the electrical properties in the upper atmosphere as proposed by Wilson. Pasko's model involves using the electron's number density and the ionization and attachment coefficients in order to calculate the conductivity of the region. Equations for these variables where developed based on measured data and the previous work by Papadopoulos et al [38]. This conductivity profile provides a more realistic estimate of the electric fields and energy dissipation.

Pasko also describes what he calls the characteristic air breakdown field, the point at where the electric field will cause the air to breakdown electrically [36, 37, 39, 40]. It is when the electric field exceeds this breakdown threshold ionization occurs, which according to Wilson will allow an electrical discharge. As altitude increases, this characteristic breakdown field decreases in magnitude, which confirms Wilson's theory of a smaller electric field being necessary at higher elevations [33].

Barrington-Leigh [40] provided a modified set of equations for the ionization and attachment coefficients. These equations offer slight differences from those given by Pasko but are less numerically cumbersome and will be used in the work presented in this

research. The atmospheric electron number density and ambient conductivity values provided by Pasko will be used.

1.4.4 Additional Numerical Methods

There have been many other numerical methods developed to simulate the effects of a lightning perturbation on the upper atmosphere. Taranenko et al. developed a model based on electron dynamics and Maxwell's equations to determine the excitation of optical emissions [41]. Like Pasko's work, this was based on the heating of electrons due to changes in the electron density. It showed an increase in ionization at altitudes greater than 85 km with a decrease below that altitude [11].

A "particle model" based on a quasi-electrostatic design was developed by Tong et al, indicating the number density of electrons can reach values doubled that of ambient conditions [6]. Transmission-line models where develop by Dowden et al. which showed that at 70 km, conductivities of over 30 μS/m and electron densities of ~ 10^{10} e^-/m^3 are needed for sprite development [42, 43].

1.5 Thesis Outline

The remainder of this thesis is outlined as follows. Chapter 2 presents the formulation of the equations used in this model. This includes those based on a modified form of Maxwell's equations, ambient conductivity models, and ionization equations based on prior research of Pasko [36, 37] and Barrington-Leigh [40]. Chapter 3 presents specifics of the Finite Element Model and chapter 4 includes the results of the simulations along with discussions. Chapter 5 is a summary with conclusions and possible suggestions for future work.

CHAPTER 2

PROBLEM FORMATION

2.1 Overview

In this chapter equations are derived based on a modified form of Maxwell's equations and atmospheric constitutive parameters which will describe the effects of ionization on the atmosphere resulting from the reconfiguration of charge due to a lightning event. Equations describing the ambient ion conductivity are presented followed by those that will simulate the effect that the electric field has on the electron component of the conductivity. If significant ionization occurs, this will cause photon emissions in the optical band [7, 36-37]. Therefore, identification of significant ionization through modeling should identify the presence of a sprite.

2.2 Derivation from Modified Maxwell's Equations

The effects of ionization are characterized in an equation which is derived from a modified form of Maxwell's equations and atmospheric constitutive parameters. The equations used are as follows in differential form:

$$\nabla \times \mathbf{H} = \mathbf{J}_{\mathrm{C}} + \frac{\partial \mathbf{D}}{\partial t} + \mathbf{J}_{\mathrm{S}} \tag{2.1}$$

$$\mathbf{D} = \varepsilon_0 \mathbf{E} \tag{2.2}$$

$$\mathbf{J}_{\mathrm{C}} = \sigma \mathbf{E} \tag{2.3}$$

$$\nabla \cdot \mathbf{J_S} = -\frac{\partial \rho_f}{\partial t} \tag{2.4}$$

$$\mathbf{E} = -\left(\nabla \mathrm{V} + \frac{\partial \mathbf{A}}{\partial t} \right) \tag{2.5}$$

For all equations, the SI system of units is used where **H** is magnetic intensity (A/m), **D** is the electric flux density (C/m^2), **E** is the electric field (V/m), V is the electric potential (V), $\mathbf{J_S}$ is the source current density associated with the return stroke current (A/m^2) [44-46], $\mathbf{J_C}$ is the conduction current density (A/m^2) [47], σ is the conductivity (mho/m), ε_0 is the permittivity of free space (F/m), and ρ_f is the source charge density associated with the return stroke current (C/m^3). As study focuses on the late-time component of the sprite, a quasi-static problem is assumed where $d\mathbf{A}/dt = 0$ [45, 46].

The equations required for the simulation are derived from Eqns. (2.1) - (2.5) as follows: Eqns. (2.2) and (2.3) are inserted into Ampere's law (2.1) and the divergence is taken resulting in (2.6). Eqns. (2.4) and (2.5) are then applied resulting in the continuity equation (2.7).

$$0 = \nabla \cdot \left(\nabla \times \mathbf{H} \right) = \nabla \cdot \sigma \mathbf{E} + \varepsilon_0 \nabla \cdot \frac{\partial \mathbf{E}}{\partial t} + \nabla \cdot \mathbf{J_S} \tag{2.6}$$

$$\nabla \cdot \left(\sigma \nabla \mathrm{V} + \varepsilon_0 \frac{\partial \nabla \mathrm{V}}{\partial t} \right) - \frac{\partial \rho_f}{\partial t} = 0 \tag{2.7}$$

This equation is used in the Finite Element Model (FEM) discussed in Chapter 3. In the next section, the source charge density which is used to approximate the effects of the lighting discharge is developed. Afterwards, a number of conductivity profiles will be introduced, and the effects of each on the electric field signatures examined.

2.3 Modeling of Lightning Discharge

The source of a sprite event is an intense, high current lightning discharge causing charge reconfiguration [44, 49]. The model described here does not take in account the effects of the propagating fields. As mentioned earlier, this study focuses on the late-time or quasi-static field behavior [45, 46].

The total charge transferred at time t is the integral of the return stroke current given by Baginski [35, 44, 50] as:

$$Q_f(t) = \int_0^t i_R(\tau)\partial\tau \tag{2.8}$$

where $i_R(\tau)$ = lightning return stroke current
$Q_f(t)$ = total displace charge due to the return stroke

The temporal structure of this displaced charge is expressed as [35, 44, and 50]:

$$\frac{\partial Q_f(t)}{\partial t} = i_R(t) = I_0\left(\exp(-at) - \exp(-bt)\right) \tag{2.9}$$

where $a = 1 \times 10^4$ and $b = 5 \times 10^5$ s^{-1}.

The charge deposition is expressed using a modified spherical Gaussian profile provided by Baginski [44, 50]:

$$\frac{\partial \rho_f(r,z,t)}{\partial t} = \frac{\partial Q_f}{\partial t} f(r,z)$$
$$f(r,z) = \frac{\exp(-R/2\lambda)}{(2\pi\lambda)^{1.5}} \tag{2.10}$$

where

$$R = r^2 + (z - z')^2 \tag{2.11}$$

and z' is the altitude of charge perturbation (m), and λ is the standard deviation (λ = 6000 m^2). There is a large degree of latitude allowed in choosing the standard deviation as the total displaced charge is the primary factor in the electric field characteristics at the altitudes of interest [40, 44, and 50]. In this study, the positive charge center is assumed located at z' = 10 km [37, 40, 44].

2.4 Atmospheric Conductivity Modeling

The main focus of this research is to investigate the electric field signatures and ionization levels for different conductivity profiles. The total conductivity used in Eqn. (2.7) consists of two components, the positive ion and electron conductivities shown by:

$$\sigma = \sigma_i + \sigma_e \tag{2.12}$$

where σ_i is the ion conductivity and σ_e is the electron conductivity. The first profiles introduced are for standard models [35, 37, 50, 51] based on ambient ion conductivity. The model is then modified to include the enhanced electron conductivity component.

2.4.1 Standard Models

Two ambient ion conductivities profiles are used as standard baseline models. The first is the Gish model [35, 50] shown below:

$$\begin{aligned} F_1 &= 2.94/\exp\left(4.5\times10^{-3} z\right), \quad z < 4000\ m \\ F_1 &= 0, \qquad\qquad\qquad\quad z >= 4000\ m \\ F_2 &= 1.39/\exp\left(3.75\times10^{-4} z\right) \\ F_3 &= 0.369/\exp\left(1.21\times10^{-4} z\right) \\ \sigma &= 6\times10^{-14}/\left(F_1 + F_2 + F_3\right) \quad (S/m) \end{aligned} \tag{2.13}$$

The second ambient conductivity profile is a single exponential representation that has been used in numerous models given by [37, 50, and 51]:

$$\sigma_i = 5\times10^{-14}\exp(z/6km) \quad (S/m) \tag{2.14}$$

For both models, the conductivity is only a function of altitude.

Fig. 2.1 shows both ambient conductivity profiles as a function of altitude. In the area of interest, ~ 40 to 95 km in altitude, the exponential conductivity is greater than the Gish-Wait conductivity with ranging from ~ 2 x 10^{-11} to 3.6 x 10^{-7} S/m. These profiles are employed in the FEM model without accounting for the enhanced electron ionization with the results shown in Chapter 4. In the next section, the effects of ionization are included in electrical conductivity.

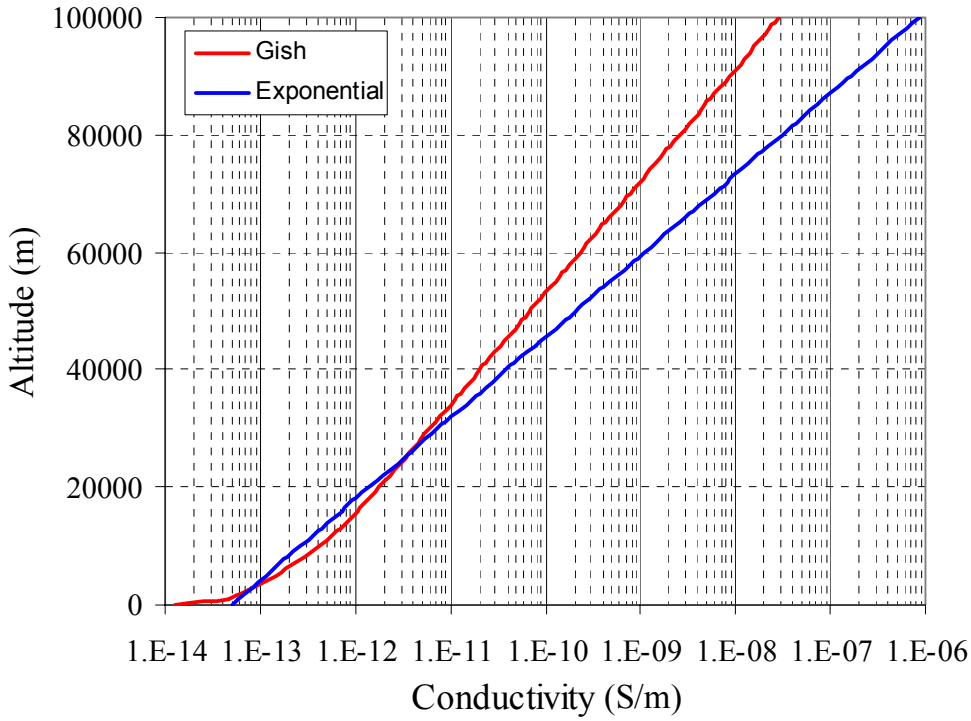

Figure 2.1 Ambient ion conductivity profiles with respect to altitude

2.4.2 General Conductivity Model

Electron ionization affects the region of atmosphere above ~ 60 km [37, 52]. The total conductivity model will first be developed for ambient conditions followed by a model that includes the effects of ionization.

2.4.2.1 Ambient Values

The electron component of the total conductivity is given by [37, 40]:

$$\sigma_e = q_e N_e \mu_e \tag{2.15}$$

where q_e is the electric charge (C), N_e is the number density of electrons (e^-/m^3), and μ_e is the mobility of electrons ($m^2/V{\cdot}s$). The average number density of 3 electron density profiles was used in this research [36, 37] and shown by Fig. 2.2. The ambient electron mobility is described for "essentially cold electrons" and given by [36, 37]:

$$\mu_e = 1.36\, N_0 / N \tag{2.16}$$

where N_0 = 2.688 x 10^{25} e^-/m^3. N is the number density of air molecules ($Atms/m^3$) and shown by Fig. 2.3 [36, 37].

A third conductivity profile is created using the exponential model and the vertical component of the conductivity for altitudes >60 km. This vertical component of the conductivity is represented by Eqn. (2.15) using the ambient values for the electron mobility and the electron density. This profile will be referred to as "profile 3". Fig. 2.4 shows the exponential conductivity model and profile 3 for altitudes up to 100 km.

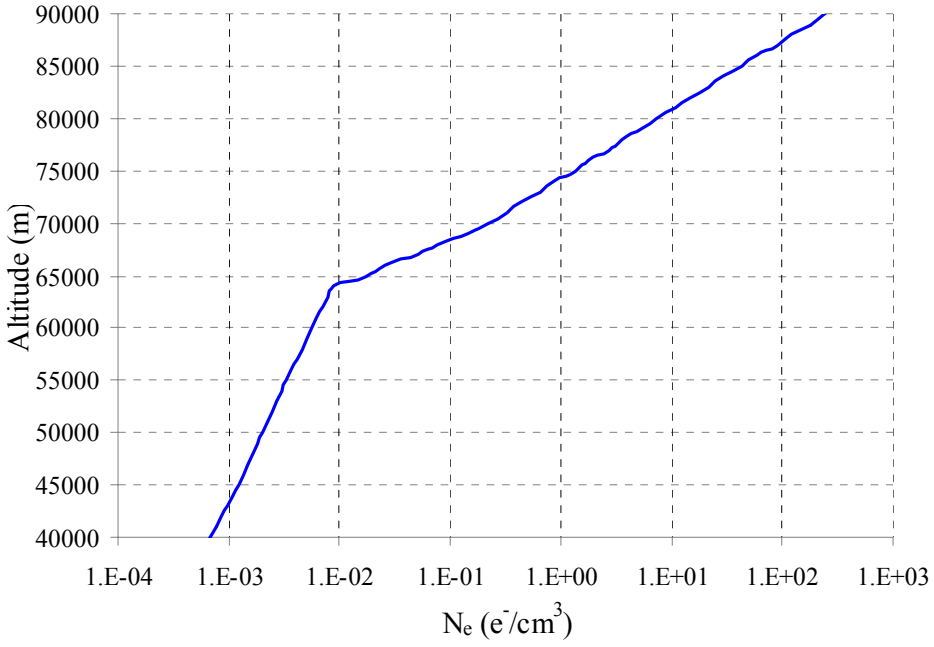

Figure 2.2: Ambient electron number density profile

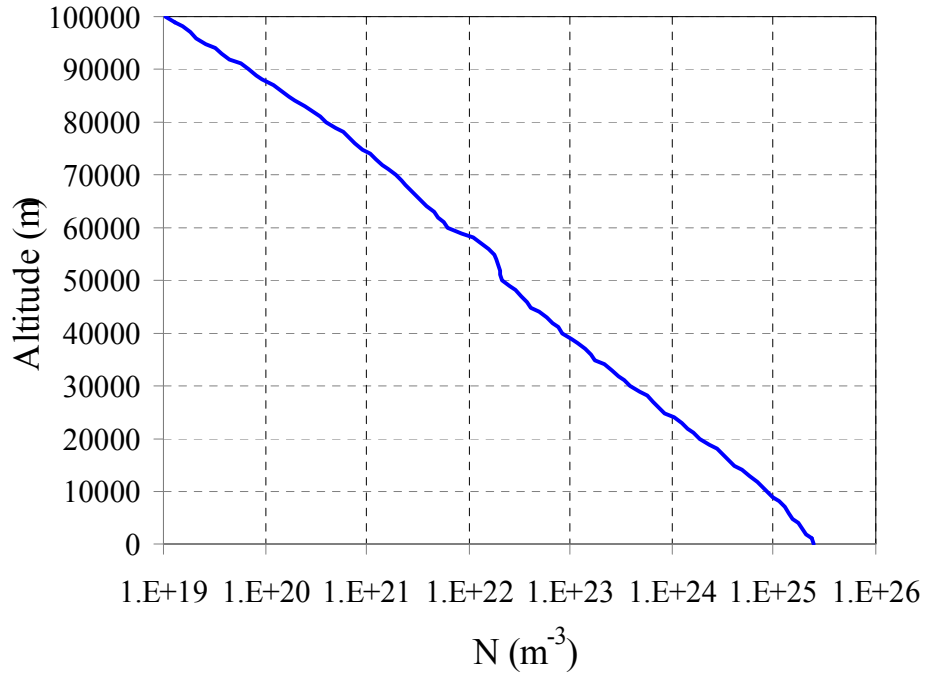

Figure 2.3: Number density of air molecules (*N*) as a function of altitude.

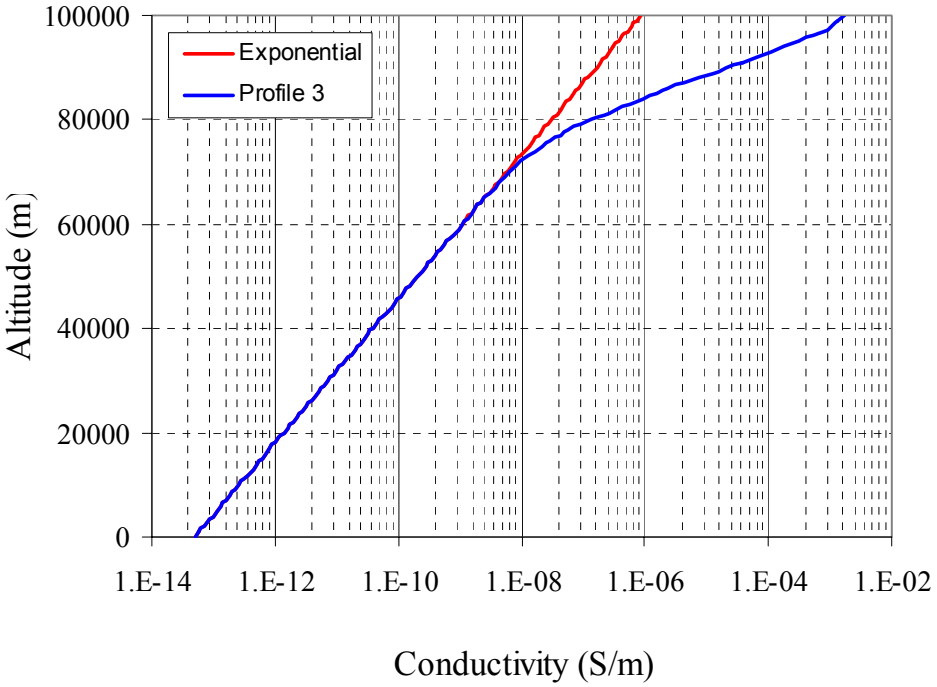

Figure 2.4: Conductivity profile as a function of altitude.

2.4.2.2 Electron Mobility

The electron mobility model is a functional fit based on experimental data and given by [36, 37]:

$$\log(\mu_e N) = \sum_{i=0}^{2} a_i x^i, \quad EN_0 / N \geq 1.62\times10^3 \quad V/m$$
$$\mu_e N = 1.36 N_0, \quad EN_0 / N < 1.62\times10^3 \quad V/m \tag{2.17}$$

where $x = \log(E/N)$, a_0 = 50.970, a_1 = 3.0260, and a_2 = 8.4733 x 10^{-2}. Fig. 2.5 shows the electron mobility for 50 and 80 km altitude as a function of electric field strength. As can be seen from the figure, for low electric field values the electron mobility tends to the ambient values.

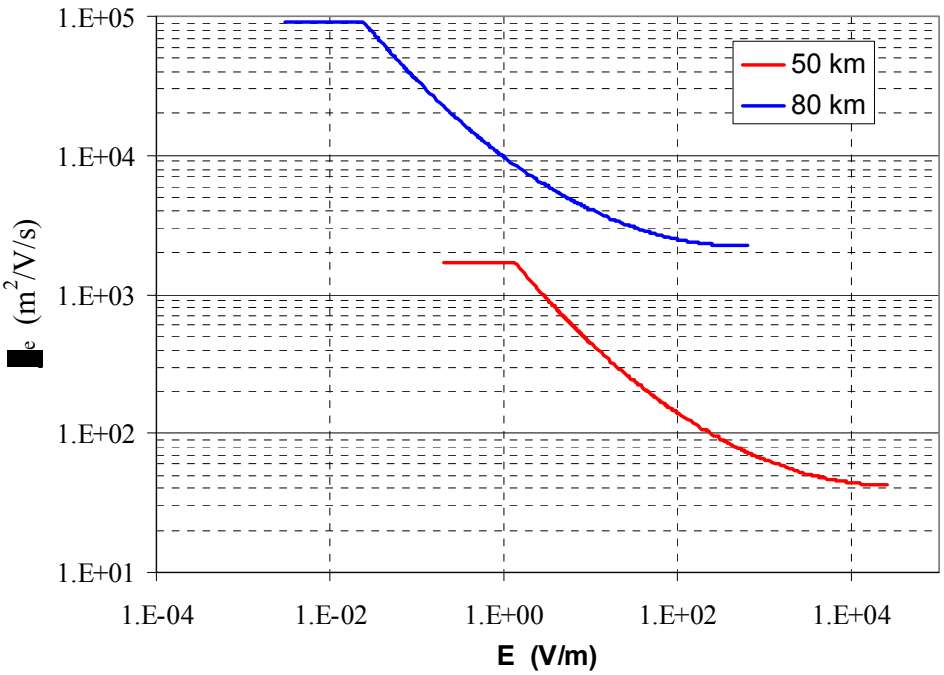

Figure 2.5: Electron mobility (μ_e) at 50 and 80 km.

2.4.2.3 Electron Density

The electron number density is described according to the following differential equation [36, 37, and 40]:

$$\frac{dN_e}{dt} = (\nu_i - \nu_a)N_e - \alpha N_e^2 \tag{2.18}$$

where ν_i is the ionization coefficient (1/s), ν_a is the attachment coefficient (1/s) and α is the effective recombination coefficient [36]. The last term of αN_e^2 is used to model the propagation channels to altitudes <50 km resulting from ionization breakdown [36]. This term is neglected in this study as the value is not well known for high altitudes and the solution becomes very numerically intensive.

2.4.2.4 Ionization and Attachment Coefficient

The ionization and attachment coefficients are solved using functions provided by Barrington-Leigh [40]. The ionization coefficient is given by:

$$\begin{aligned} \nu_i &= 0 \qquad \text{for} \frac{E}{N/N_0} < 1122000 \text{ V-m}^{-1}, \\ \nu_i &= \frac{N}{N_0} 10^P \qquad \text{otherwise}, \\ p &= \sum_{i=0}^{3} a_i \left[\log_{10}\left(\frac{E}{N/N_0} \right) \right]^i \end{aligned} \tag{2.19}$$

with a_0 = -624.68, a_1 = 239.60, a_2 = -32.878, and a_3 = 1.4546. The attachment coefficient is given by:

$$\begin{aligned} \nu_a &= 0 \qquad \text{for} \frac{E}{N/N_0} < 316200 \text{ V-m}^{-1}, \\ \nu_a &= \frac{N}{N_0} 10^P \qquad \text{otherwise}, \\ p &= \sum_{i=0}^{4} b_i \left[\log_{10}\left(\frac{E}{N/N_0} \right) \right]^i \end{aligned} \tag{2.20}$$

with a_0 = -3567.0, a_1 = 1992.68, a_2 = -416.601, a_3 = 38.7290, and a_4 = -1.35113. These coefficients are shown as a function of the electric field for altitudes of 50 and 80 km in Fig. 2.6. It is of note to mention that when compared to the electron mobility, it is not until significant electric field strengths occur before the coefficient values change the electron number density, which in turn affects the conductivity.

The electric field intensity at which $\nu_i = \nu_a$ corresponds to E_k, the characteristic air breakdown field (V/m) [40]. This breakdown field is described by the equation [36, 37]:

$$E_k = 3.2 \times 10^6 \frac{N}{N_0} \tag{2.21}$$

The electric field must exceed the electrical breakdown strength of the atmosphere, shown by Fig. 2.7, for sprites to occur [53]. Fig. 2.8 shows the net ionization (ν_i - ν_a) as a function of electric field strength at 70 km.

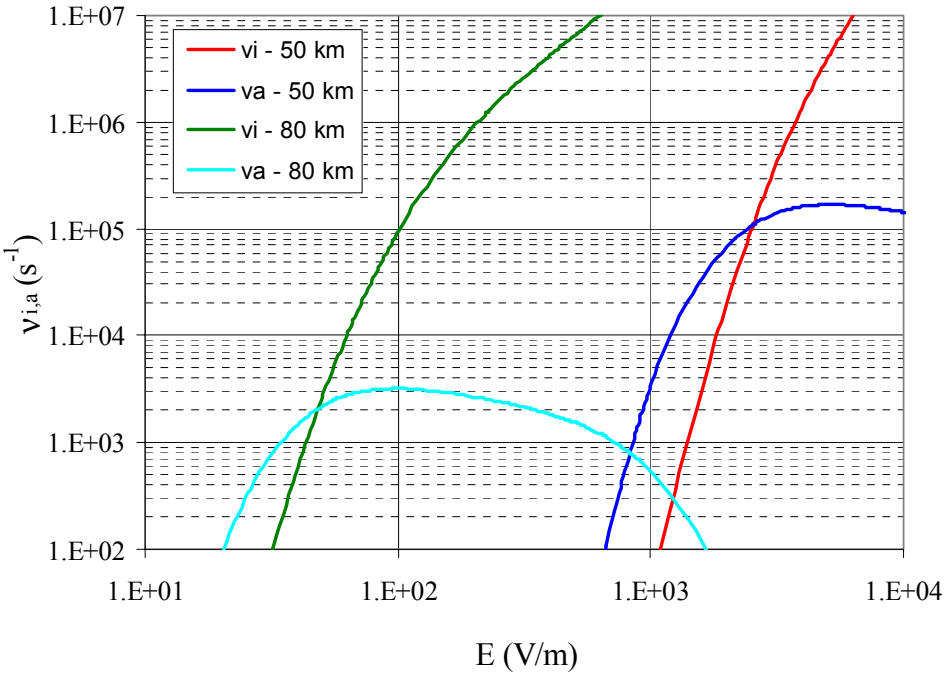

Figure 2.6: Ionization and attachment coefficients for 50 and 80 km.

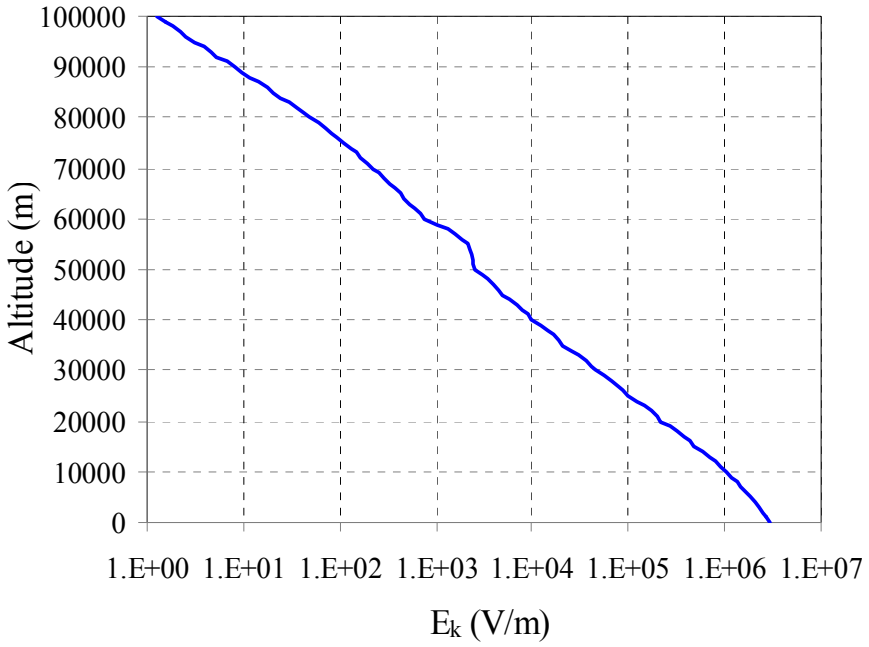

Figure 2.7: Characteristic air breakdown field with respect to altitude.

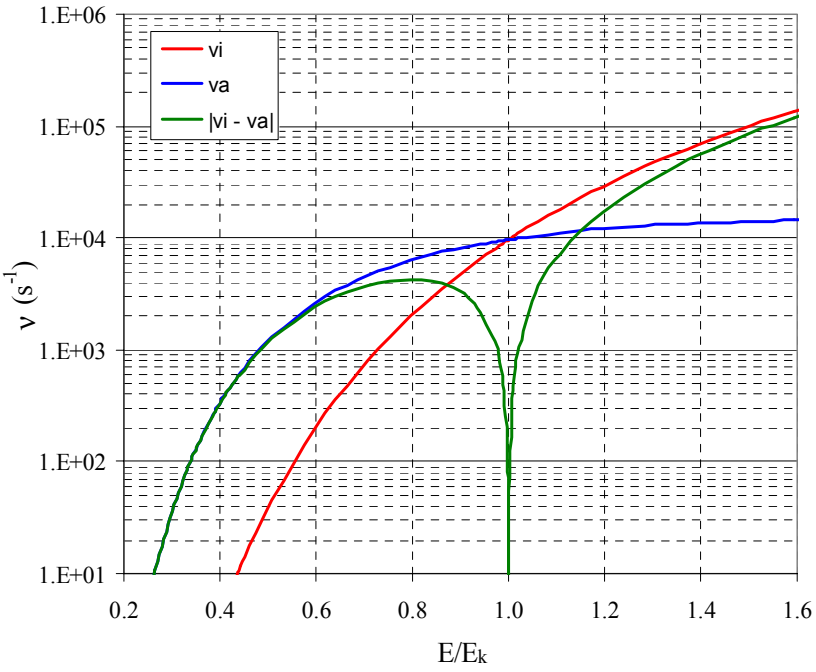

Figure 2.8: Ionization and attachment coefficients normalized to E_k for 70 km

CHAPTER 3

FINITE ELEMENT MODEL

3.1 Overview

The equations developed describing the electrical effects on the atmosphere due to a CG lightning discharge will be solved using a Finite Element Model (FEM). This will allow all the parameters to be solved simultaneously as opposed to using an iterative approach as done in previous research. In this chapter, Eqn. (2.7) will be modified to the form used in the code. The geometry of the region will then be described along with the corresponding boundary conditions used. The FEM will be solved using cylindrical coordinates.

3.2 Development of Equation

Equation 2.7 is described in cylindrical coordinates as follows:

$$\nabla \cdot \left(\sigma \nabla \mathrm{V} + \varepsilon_0 \frac{\partial \nabla \mathrm{V}}{\partial t} \right) - \frac{\partial \rho_f}{\partial t} = 0 \tag{3.1}$$

Using the following vector identities

$$\nabla \cdot \mathbf{A} = \frac{1}{\rho} \frac{\partial}{\partial \rho} \left(\rho A_\rho \right) + \frac{1}{\rho} \frac{\partial A_\phi}{\partial \phi} + \frac{\partial A_z}{\partial_z} \tag{3.2}$$

$$\nabla \cdot \left(w\mathbf{A} \right) = w \nabla \cdot \mathbf{A} + \mathbf{A} \cdot \nabla w \tag{3.3}$$

(3.1) is the differential form of the equation describing the electrical behavior of the atmosphere when subject to charge perturbations. The region for the FEM is assumed to be azimuthally symmetric about the z-axis, resulting in all derivatives with respect to ϕ going to zero.

$$\frac{1}{\rho}\frac{\partial(\rho \mathrm{A})}{\partial \rho}+\frac{\partial \mathrm{B}}{\partial z}+\frac{\partial \rho_f}{\partial t}=0$$
$$\mathrm{A}=\sigma\frac{\partial \mathrm{V}}{\partial \rho}+\varepsilon_0\frac{\partial^2 \mathrm{V}}{\partial \rho\,\partial t}$$
$$\mathrm{B}=\sigma\frac{\partial \mathrm{V}}{\partial z}+\varepsilon_0\frac{\partial^2 \mathrm{V}}{\partial z\partial t} \qquad (3.4)$$

3.3 Geometry of the Region

The FEM will be solved in a region depicted by a cylinder with a radius of 80 km and a height of 95 km (Fig. 3.1) consistent with earlier models [35, 44, and 50].

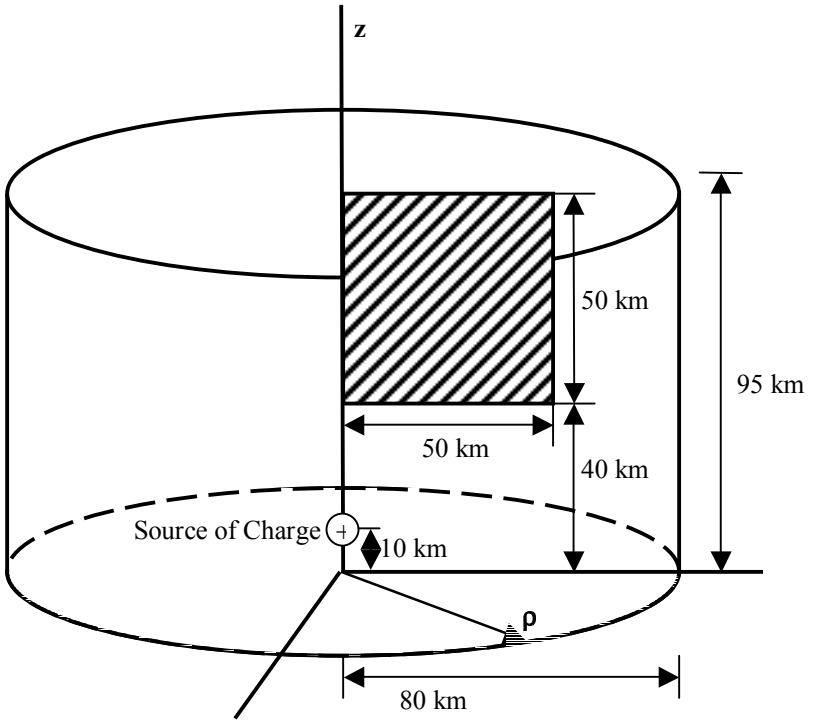

Figure 3.1: Geometry of model. Filled square denote points at which measurements are recorded.

3.3.1 Boundary Conditions

Upper and Lower Boundaries – The lower boundary of the earth's surface is modeled as a perfect electrical conductor. With the earth's surface having conductivity values of 10^{-3} to 10^{-2} S/m and the atmosphere having values of 10^{-14} to 10^{-13} S/m [44, 50]. This is a difference of at least 10 orders of magnitude makes the earth's surface appear as a perfect electrical conductor.

The upper boundary is assumed to be a perfect electrical conductor. The approximation of 95 km is appropriate since the simulations of interest are at lower altitudes and the conductivity is increasing at approximately an exponential rate. Tests have shown that increasing this boundary does not result in significant differences in the electric field in the area of interest. For both the upper and lower boundary, the horizontal electrical fields are set equal to zero and the electron number density is set to the ambient values.

Outer Boundary – The outer radial boundary extends out to 80 km. While this distance is not limited by any physical constraint, the accuracy of the FEM's solution will be greater if the discretized volume is kept to a minimum. Simulations have shown that increasing this boundary past 80 km does not result in differences in the area of interest.

3.4 Additional FEM Parameters

Two additional parameters defined in the FEM include the density of the triangulation (mesh) and the time step. The triangulation defines the step sizes and the limits of the model.

The triangulation density controls both the number and relative density of the mesh. The area where the mesh density is the greatest is in the proximity of the charge

perturbation. As the distance increases from the charge center, the triangle density steadily decreases. The mesh density is also increased in the vicinity of the sprite event (60-90 km.)

To determine the acceptable number of triangles to be used in the FEM simulation, multiple runs were conducted and the results compared. The simulations included runs with the number of triangles ranging from 1000 to 4000 triangles in 1000 triangle increments. While there were differences in the results from 1000 to 3000 triangles, it was determined that between 3000 and 4000 triangles, the differences were negligible and therefore 3000 triangles was chosen.

The time step used in the simulation is determined by both the duration of the simulation and the required number of time steps to accurately simulate the event. The minimum time step used was 10^{-8} seconds with a duration of 100 seconds. The maximum time used is 100 seconds as it was determined that this allowed the equations to run its course in the model. The simulations were divided into multiple runs, each consisting of 100 steps per decade (i.e., 10^{-2}-10^{-1} has 100 time steps). This allows for very accurate short time analysis without prohibitively long simulations.

CHAPTER 4

SIMULATION RESULTS

4.1 Overview

The FEM results are presented in two sections with figures and comments given for both. The first section contains results those for the cases where the ambient conductivity profiles were used. Simulations of the total electric field in addition to the horizontal and vertical components are shown in Figs. 4.2-4.22.

The second section contains the results for the case of where the ionization is included in conductivity calculations. The simulated electric fields, conductivity profiles, electron number densities, electron mobilities, and the ionization and attachment coefficients are shown in Figs. 4.23-4.64.

4.2 Ambient Conductivity Profiles

The three ambient conductivity profiles used in the research are shown in Fig. 4.1. They include the Gish profile, the exponential profile, and "profile 3" which includes high altitude electron ionization.

4.2.1 Total Electric Field Results

Figs. 4.2-4.7 present the simulated electric fields at a radial distance of 10 km and altitudes of 40-90 km. Each of these plots contrasts the effects of the various conductivities. The results for an altitude of 70 km and radial distances of 0-50 km are

shown in Figs. 4.8-4.10. Characteristics of the simulations are given below with discussed explanations.

1. The Gish model has a significantly lower conductivity than the other models [35, 50] and, as expected, the associated electric fields have a longer temporal duration.
2. As the altitude increases, the peak magnitude of the electric fields occurs at earlier times. At a given altitude, the peak value of the electric field occurs at approximately the same time [Figs. 4.8-4.10].
3. The peak magnitude and duration of the electric field decreases as the altitude increases for all profiles.
4. For altitudes of 40 and 50 km, the electric fields are virtually identical for the exponential conductivity model and "profile 3". This is due to the electron ionization only modifying the conductivity at altitudes $\gtrsim$ 60 km.
5. At the altitudes of 80 and 90 km, the peak value of the electric field for the simulation using the Gish conductivity exceeds the other.

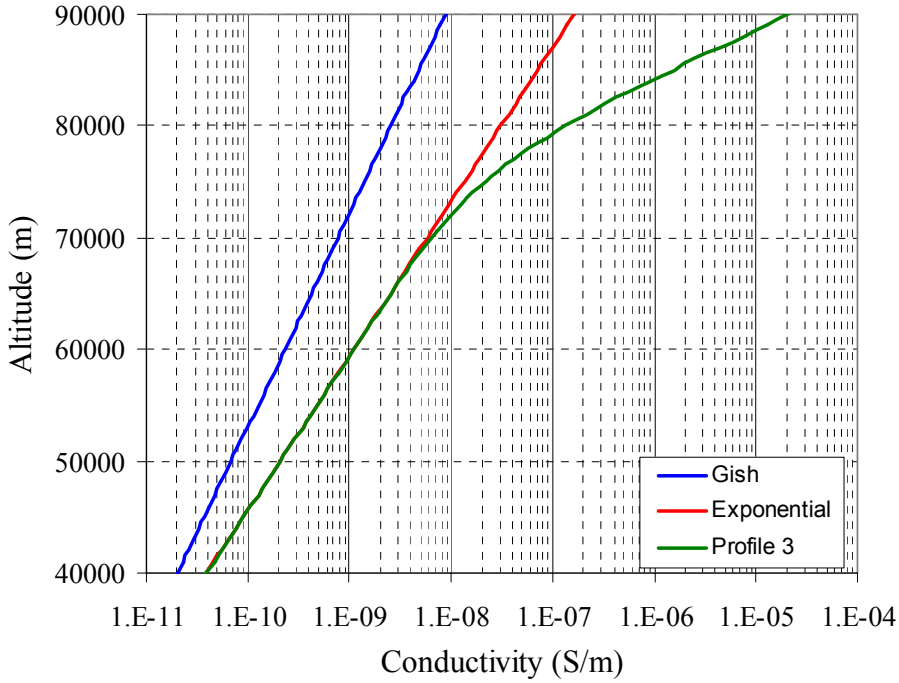

Figure 4.1: Conductivity profiles for ambient simulations

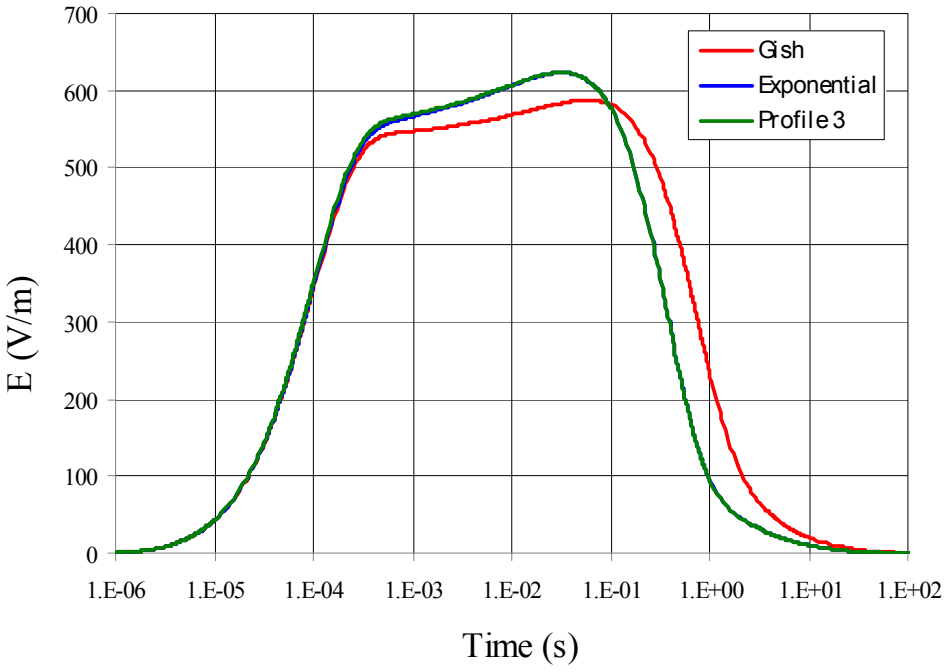

Figure 4.2: Electric field simulations at z = 40 km and ρ = 10 km for ambient conductivity profiles.

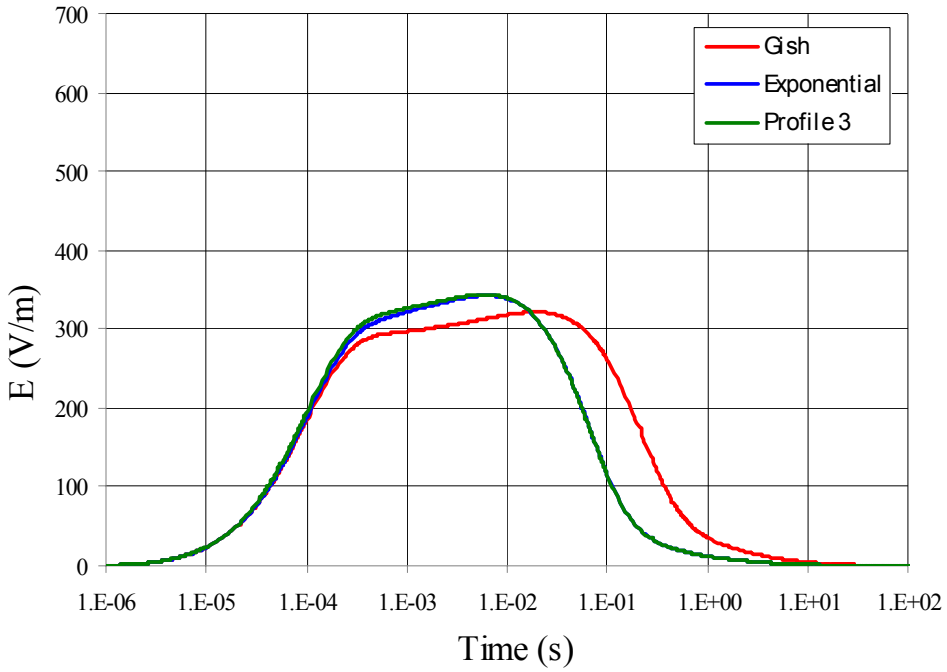

Figure 4.3: Electric field simulations at z = 50 km and ρ = 10 km for ambient conductivity profiles.

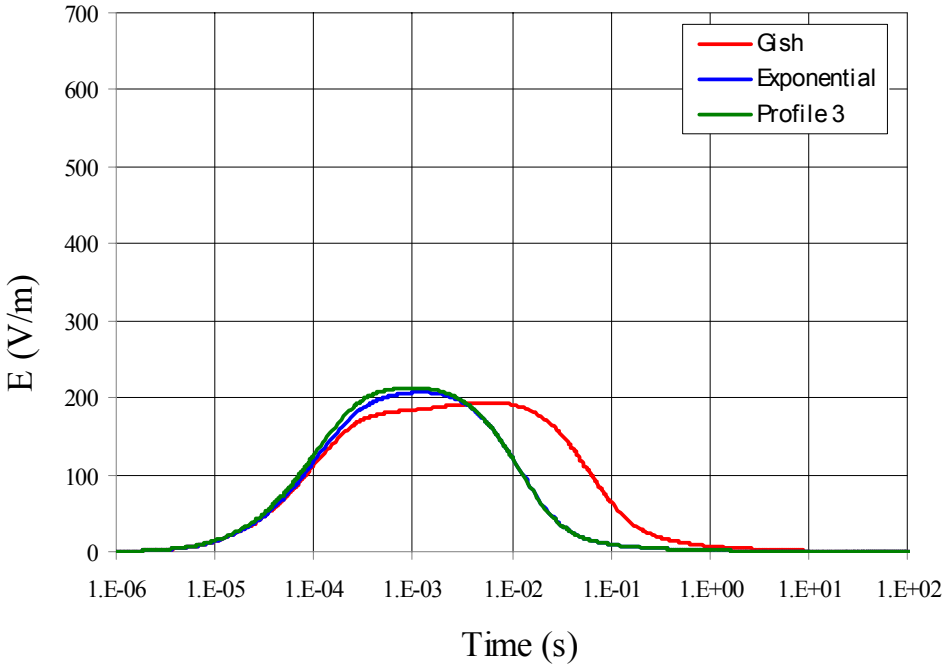

Figure 4.4: Electric field simulations at z = 60 km and ρ = 10 km for ambient conductivity profiles.

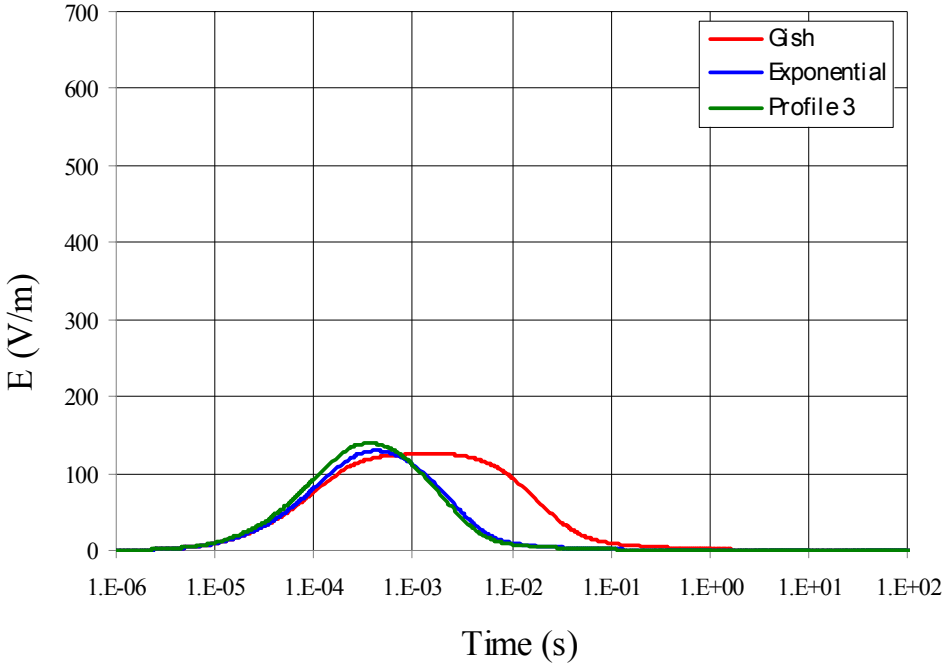

Figure 4.5: Electric field simulations at z = 70 km and ρ = 10 km for ambient conductivity profiles.

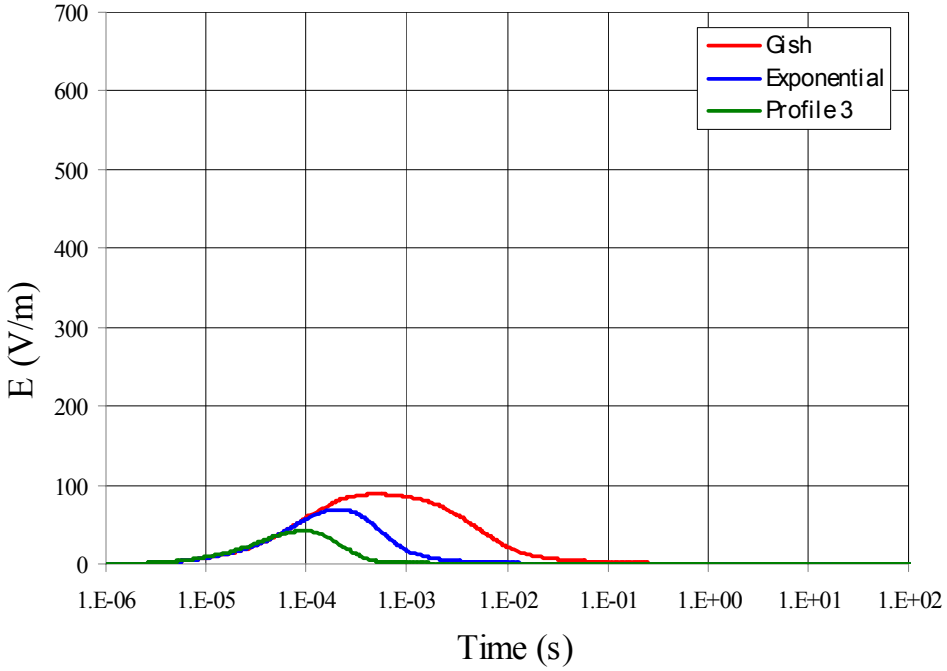

Figure 4.6: Electric field simulations at z = 80 km and ρ = 10 km for ambient conductivity profiles.

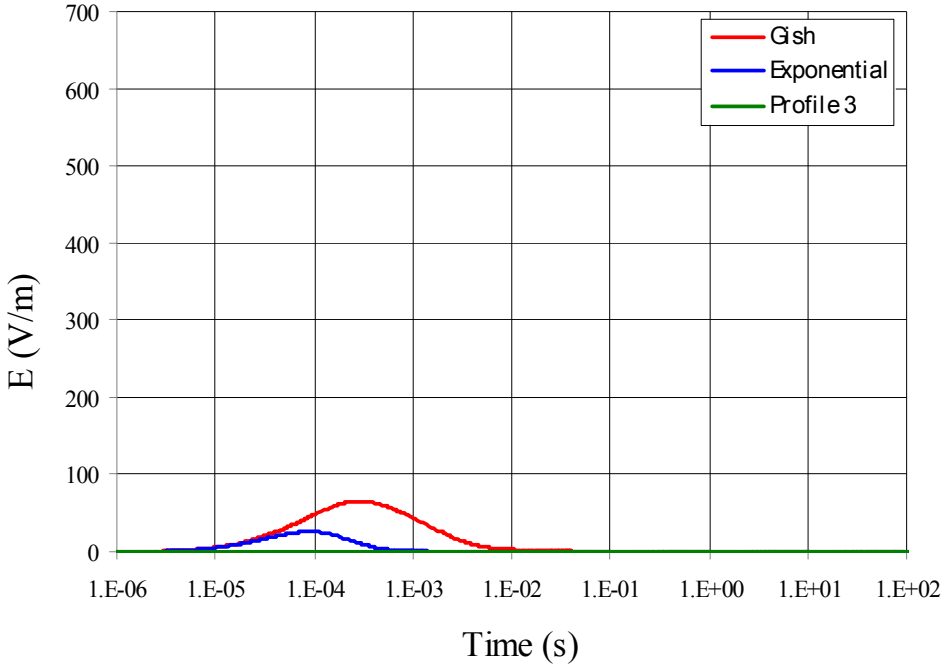

Figure 4.7: Electric field simulations at z = 90 km and ρ = 10 km for ambient conductivity profiles.

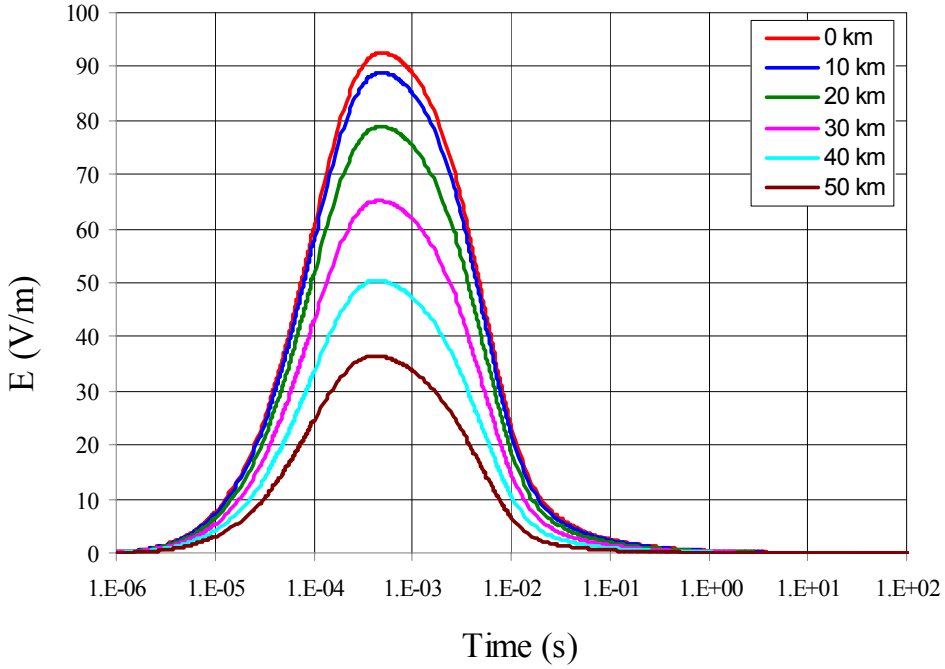

Figure 4.8: Electric field simulation using Gish conductivity profile at z = 80 km for radial distances from 0 to 50 km.

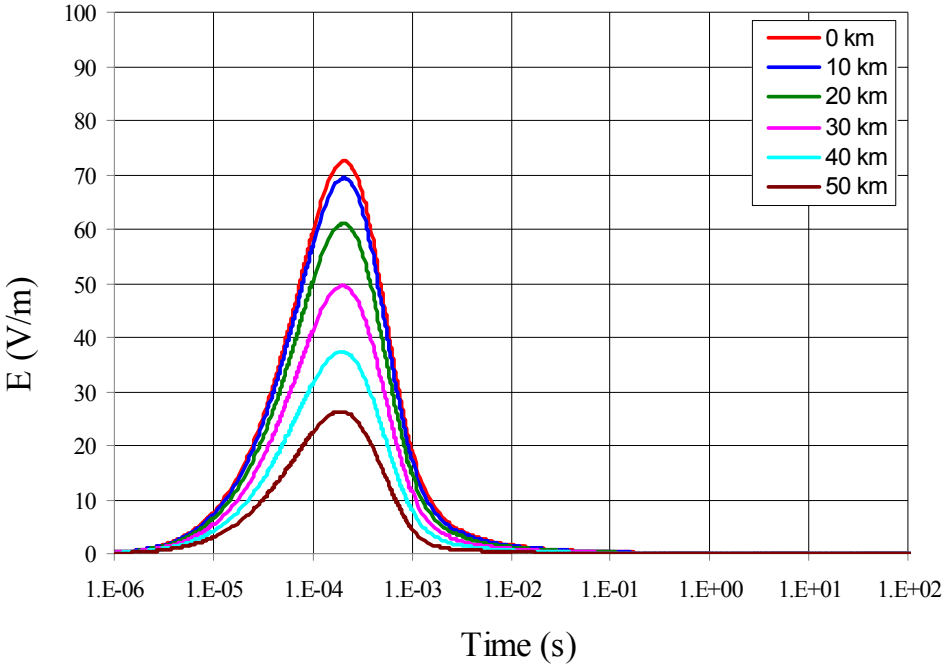

Figure 4.9: Electric field simulation using exponential conductivity profile at z = 80 km for radial distances from 0 to 50 km.

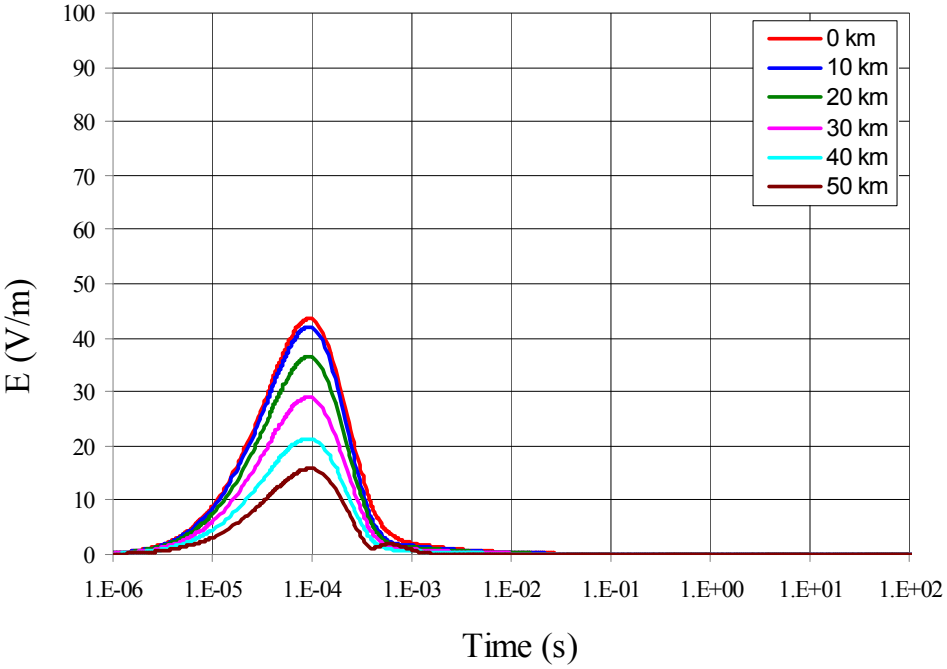

Figure 4.10: Electric field simulation using profile 3 at z = 80 km for radial distances from 0 to 50 km.

4.2.2 Vertical and Horizontal Electric Field Results

The vertical and horizontal electric fields at a radial distance of 10 km and an altitude of 40 km are shown in Figs. 4.11 and 4.12 respectively. Figs. 4.13-4.21 show the horizontal and vertical electric fields at altitudes of 40 and 80 km and radial distances from 0-50 km for the various conductivity models. Some of the noteworthy characteristics of these simulations are described below.

1. For all altitudes and radii of interest, the peak magnitudes of the vertical electric fields are greater than those of the horizontal electric fields.
2. Unlike the vertical electric fields, the peak magnitudes of the horizontal electric fields do not occur on the radial axis. At 40 km altitude, the peak magnitude of the electric field occurs at a radial distance of ~ 20 km. For 80 km altitude, the peak value of the electric field occurs between 30 and 40 km.
3. At an altitude of 80 km and radial distance of 50 km, the horizontal electric fields show a temporary field reversal for “profile 3”.
4. The horizontal electric field magnitudes are not strongly affected by the conductivity profiles while the temporal effects are similar to that of the vertical electric fields.

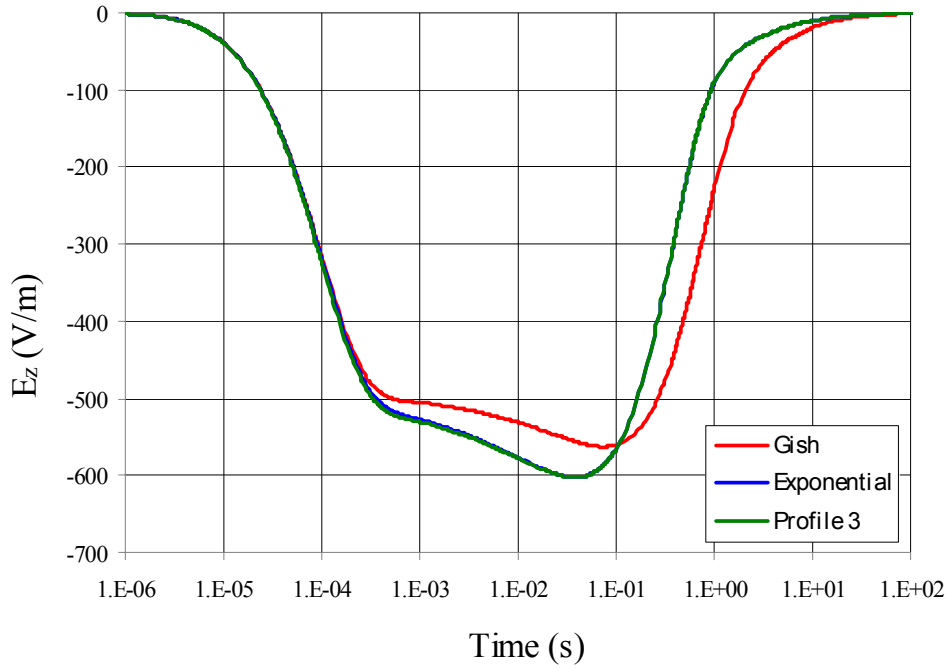

Figure 4.11: Vertical electric field simulations at z = 40 km and ρ = 10 km for ambient conductivity profiles.

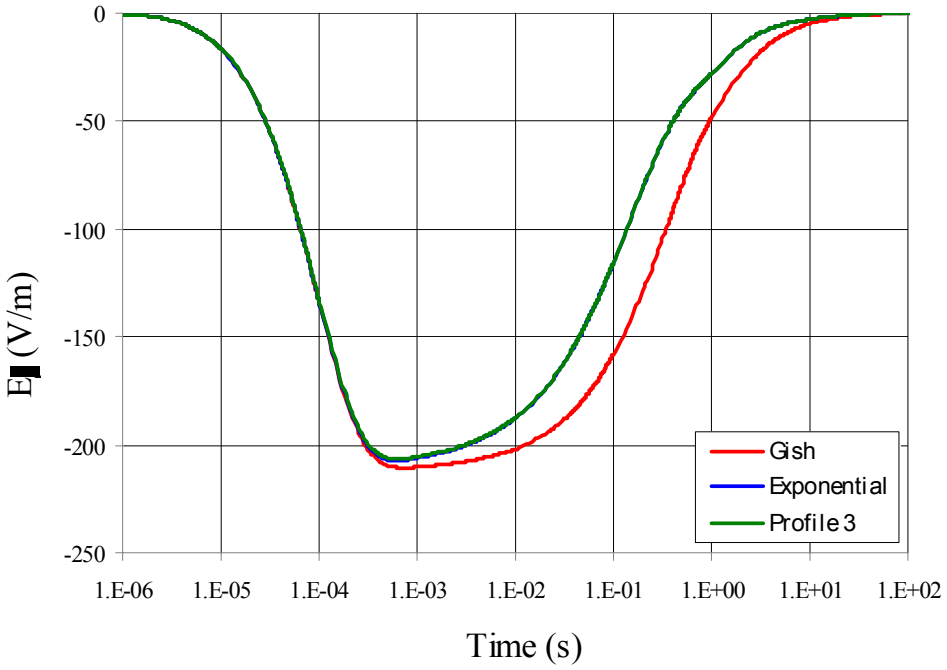

Figure 4.12: Horizontal electric field simulations at z = 40 km and ρ = 10 km for ambient conductivity profiles.

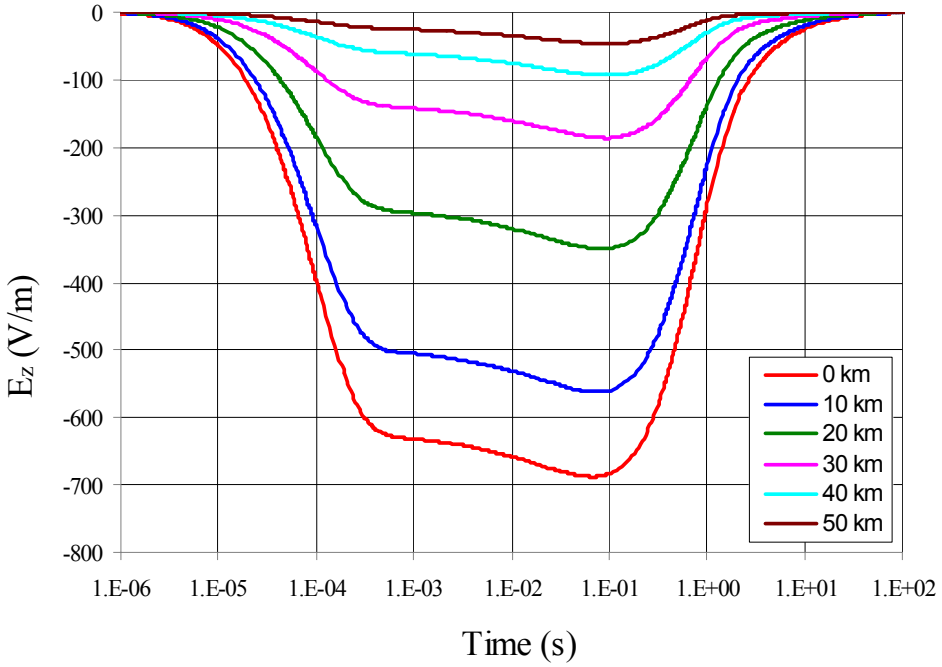

Figure 4.13: Vertical electric field simulation using Gish conductivity profile at z = 40 km for radial distances from 0 to 50 km.

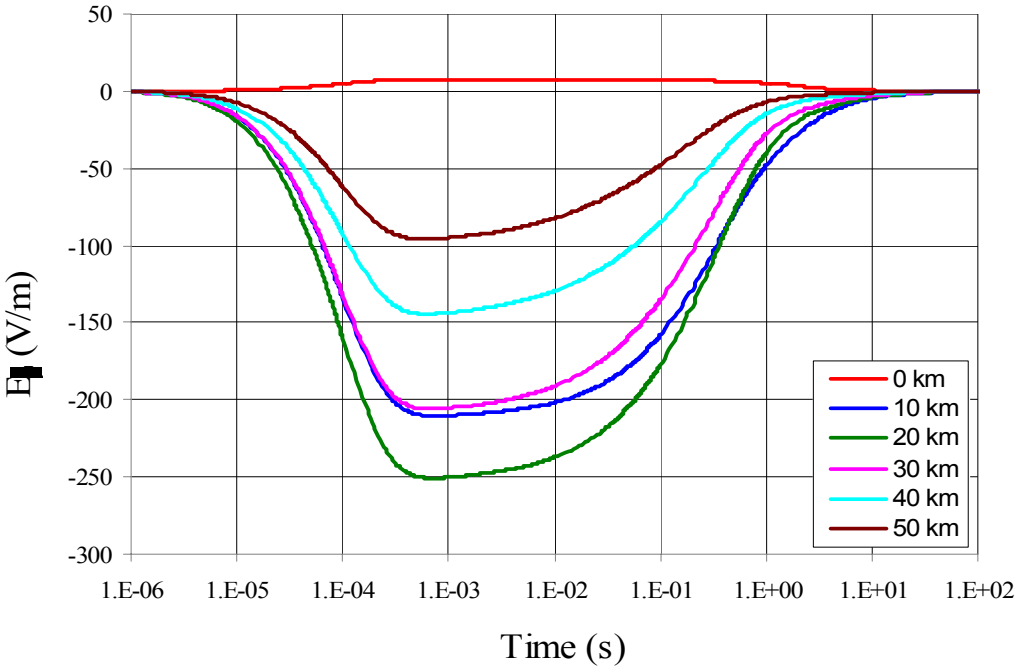

Figure 4.14: Horizontal electric field simulation using Gish conductivity profile at z = 40 km for radial distances from 0 to 50 km.

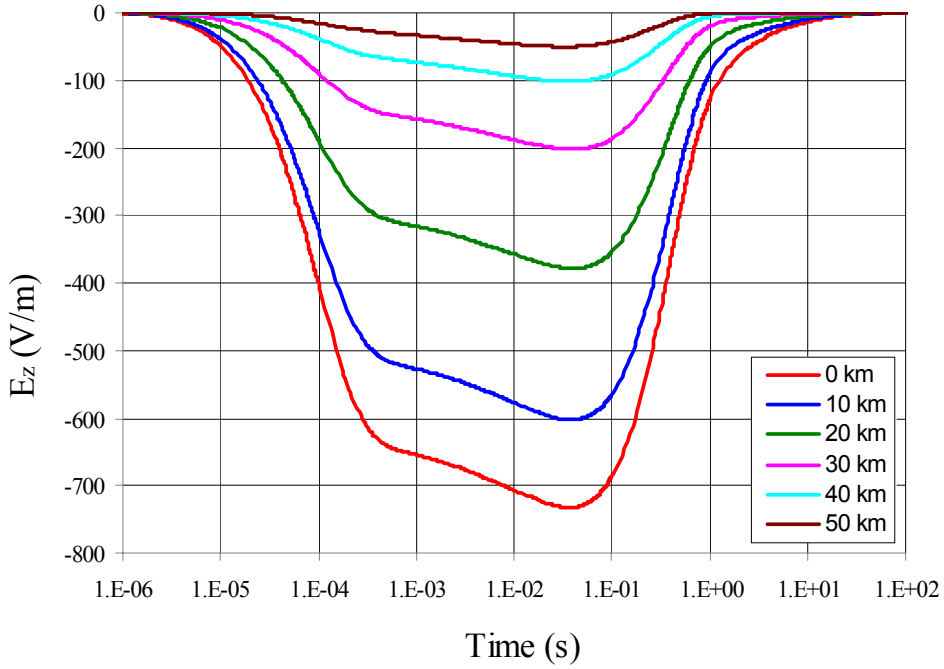

Figure 4.15: Vertical electric field simulation using exponential conductivity profile at z = 40 km for radial distances from 0 to 50 km.

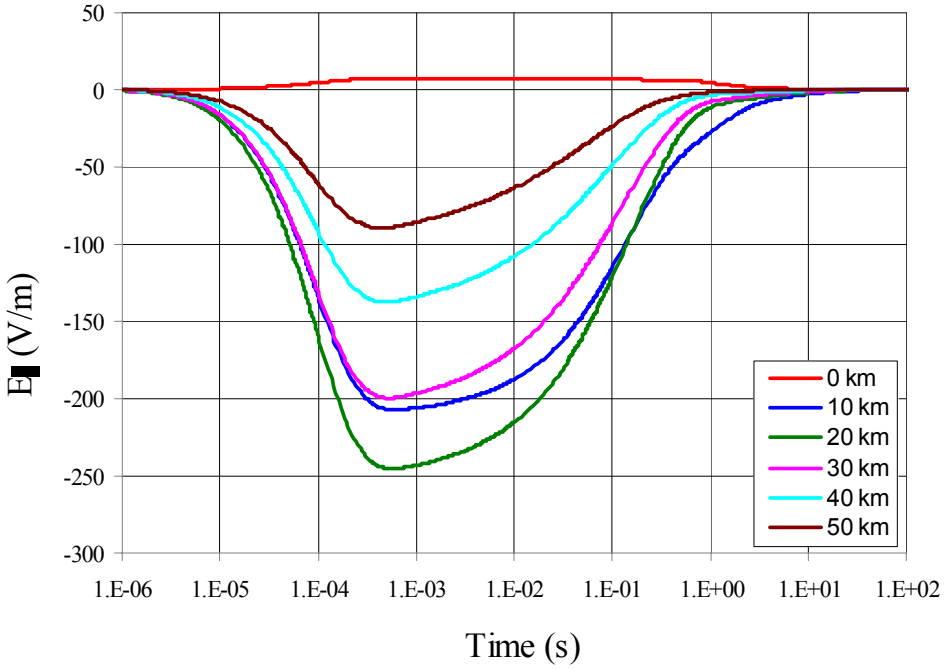

Figure 4.16: Horizontal electric field simulation using exponential conductivity profile at z = 40 km for radial distances from 0 to 50 km.

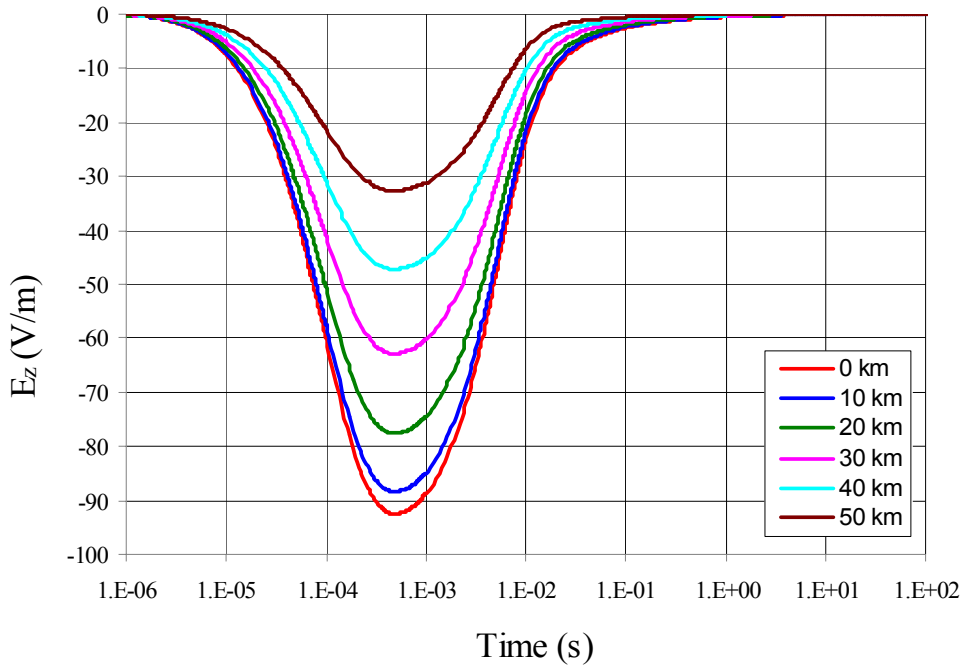

Figure 4.17: Vertical electric field simulation using Gish conductivity profile at z = 80 km for radial distances from 0 to 50 km.

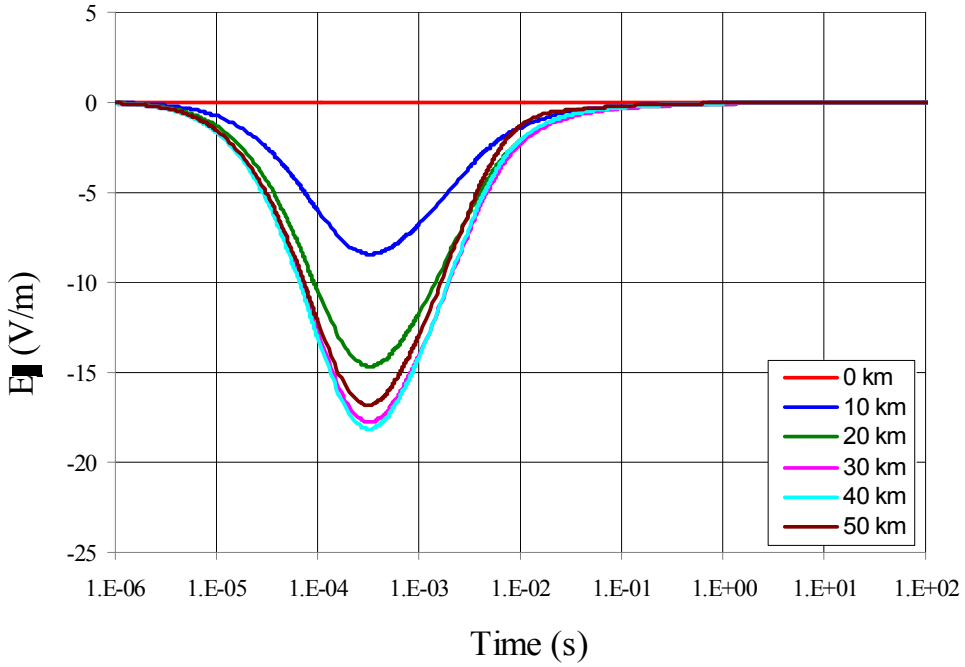

Figure 4.18: Horizontal electric field simulation using Gish conductivity profile at z = 80 km for radial distances from 0 to 50 km.

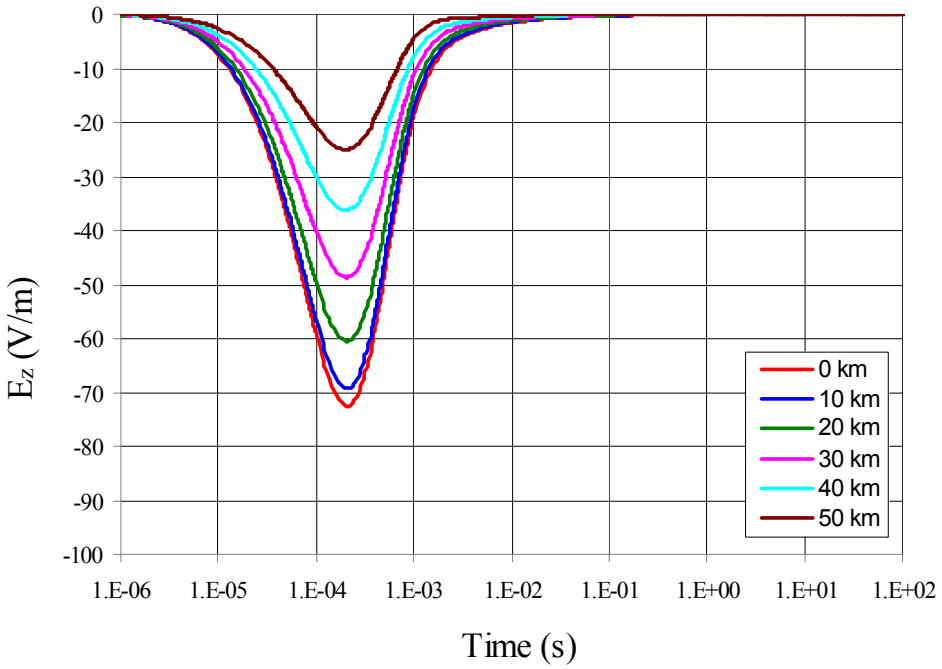

Figure 4.19: Vertical electric field simulation using exponential conductivity profile at z = 80 km for radial distances from 0 to 50 km.

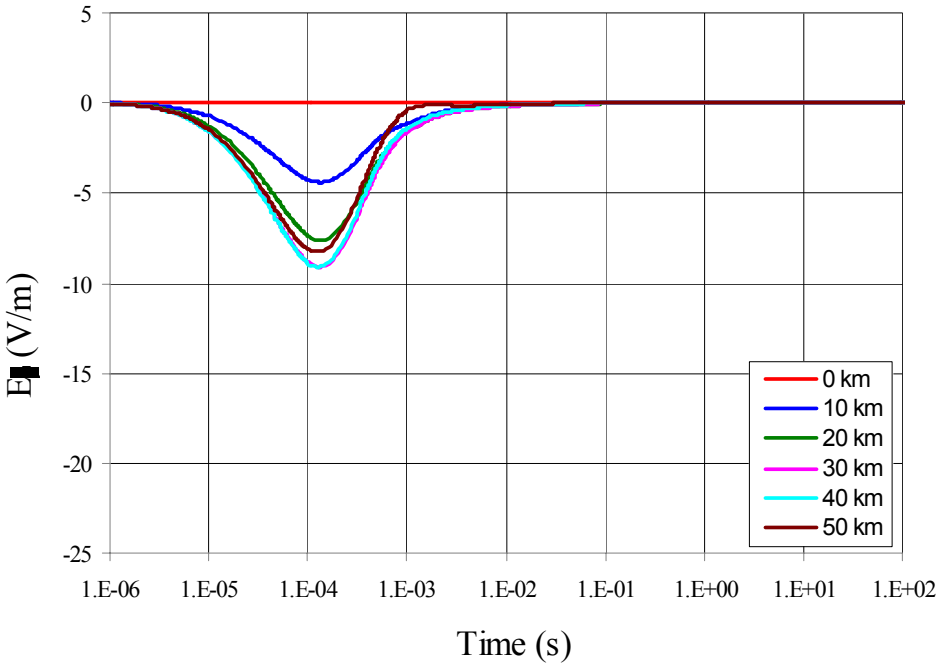

Figure 4.20: Horizontal electric field simulation using exponential conductivity profile at z = 80 km for radial distances from 0 to 50 km.

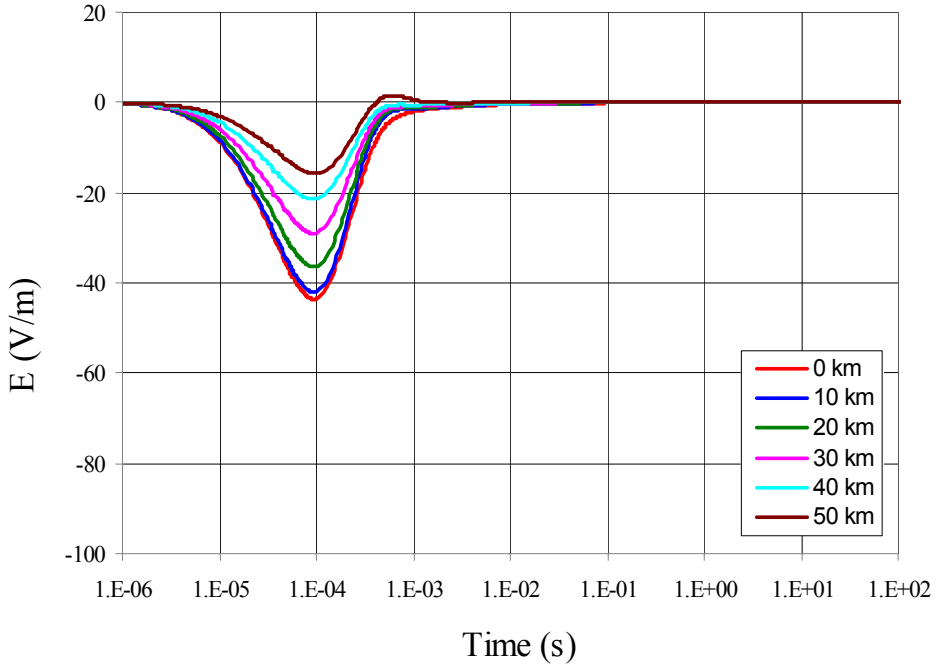

Figure 4.21: Vertical electric field simulations using profile 3 at z = 80 km for radial distances from 0 to 50 km.

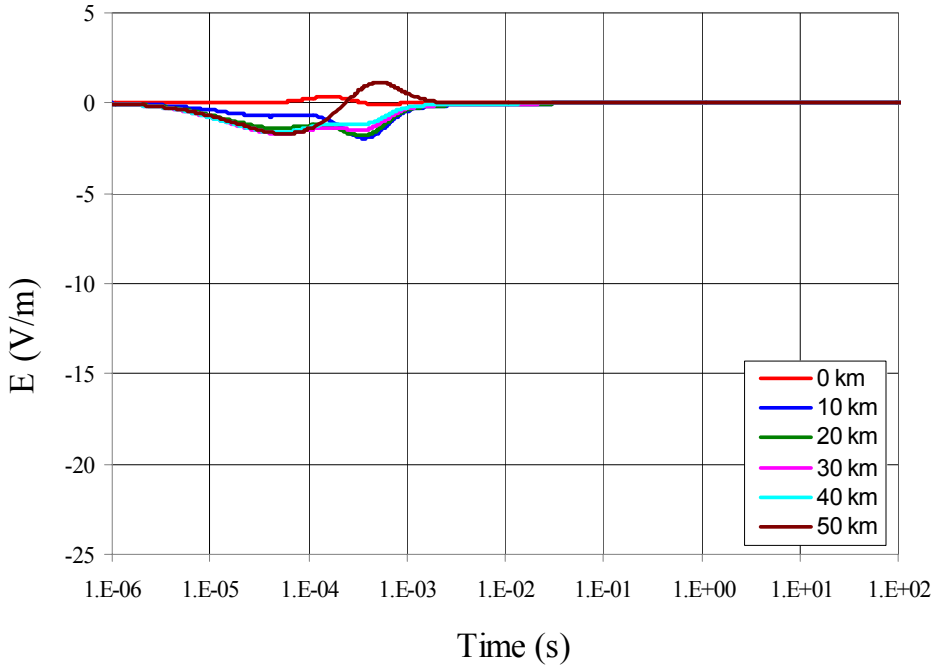

Figure 4.22: Horizontal electric field simulations profile 3 at z = 80 km for radial distances from 0 to 50 km.

4.3 Non-Linear Conductivity

In this section, electric fields, conductivities, electron mobilities, electron number densities, and ν_i and ν_a resulting from CG lightning are presented for the non-linear conductivity discussed in Section 2.4.2. All simulations presented in this section will be with respect to the non-linear conductivity and limited As stated earlier, the level of electron ionization does not modify the conductivity at altitudes below 60 km; therefore all simulations presented in this section will be limited to altitudes from 60-90 km and will be with respect to the non-linear conductivity profile.

4.3.1 Total Electric Field Results

Figs. 4.23-4.28 show the electric field simulations for a constant radial distance at altitudes varying from 60-90 km. Figs. 4.29-4.32 show the electric field simulations at a constant altitude for radial distances of 0-50 km. Figs. 4.33-4.34 show comparisons of these simulations to the electric field signatures found using the exponential conductivity model. Following are some characteristics of the electric fields:

1. Fig. 4.31 shows the rate of decay of the electric field for an altitude of 80 km is more rapid closer to the radial axis. For the other altitudes this trend is not observed.
2. Fig. 4.33 shows that the value of the peak electric field is larger for the non-linear conductivity simulations than the ambient exponential conductivity simulations at 80 km altitude. The rate of decay of the electric field following the onset of the peak value is greater for the non-linear case.
3. Fig. 4.34 compares the electric fields for the non-linear conductivity profile and the exponential conductivity model at 0.5 ms at a radial distance of 0 km. The

non-linear conductivity's peak electric field is larger at altitudes less than ~ 75 suggesting the high altitude ionization effectively "shorts" the electric field.

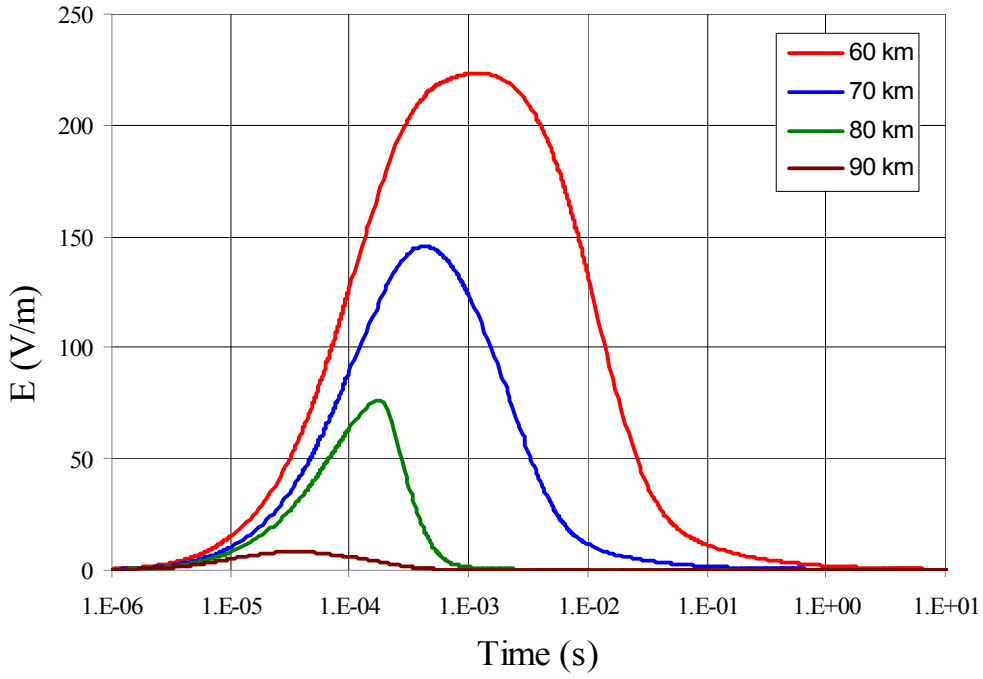

Figure 4.23: Electric field simulations using the non-linear conductivity profile for ρ = 0 km at altitudes of 60-90 km.

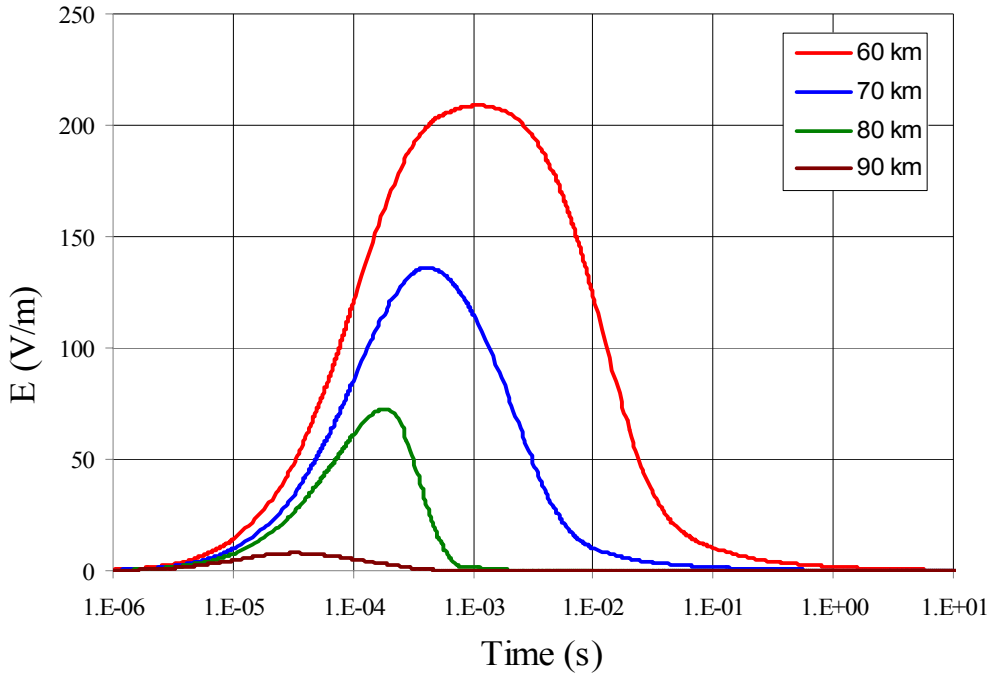

Figure 4.24: Electric field simulations using the non-linear conductivity profile for ρ = 10 km at altitudes of 60-90 km.

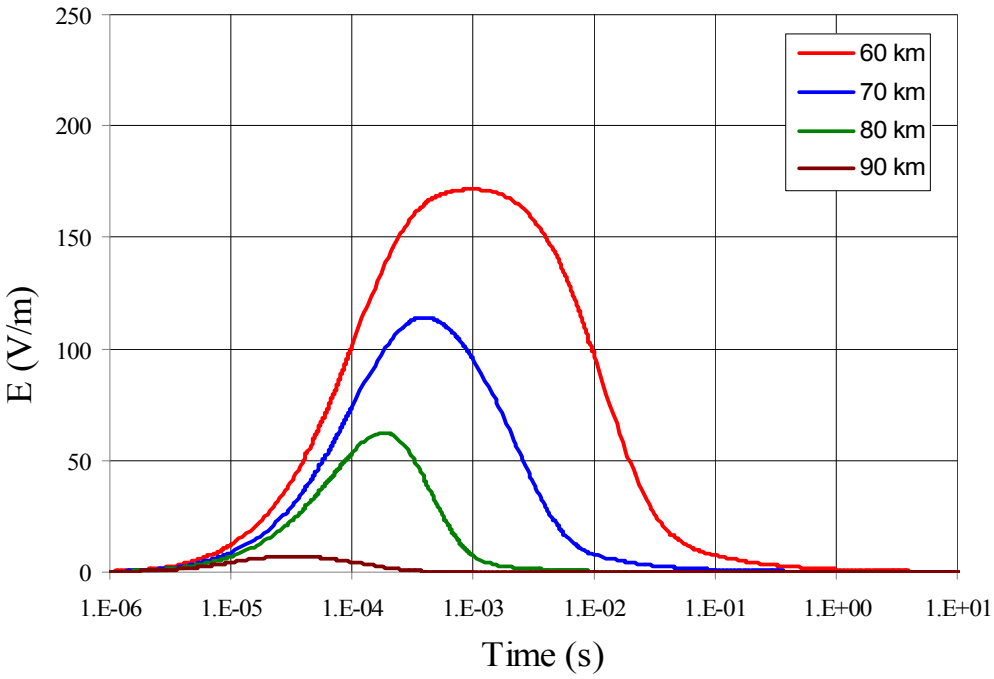

Figure 4.25: Electric field simulations using the non-linear conductivity profile for ρ = 20 km at altitudes of 60-90 km.

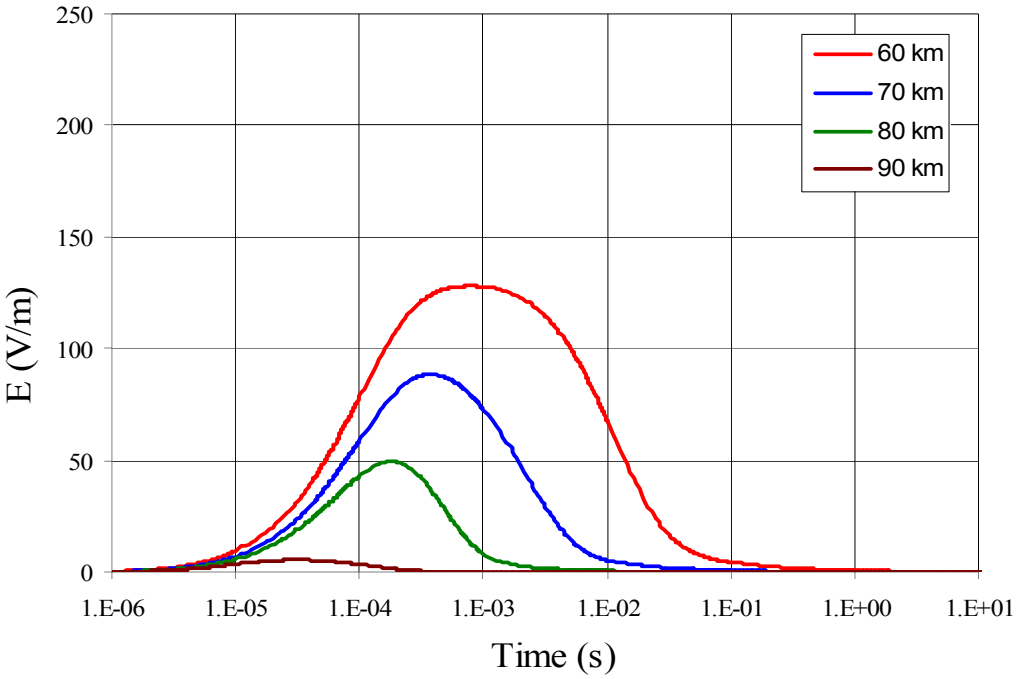

Figure 4.26: Electric field simulations using the non-linear conductivity profile for ρ = 30 km at altitudes of 60-90 km.

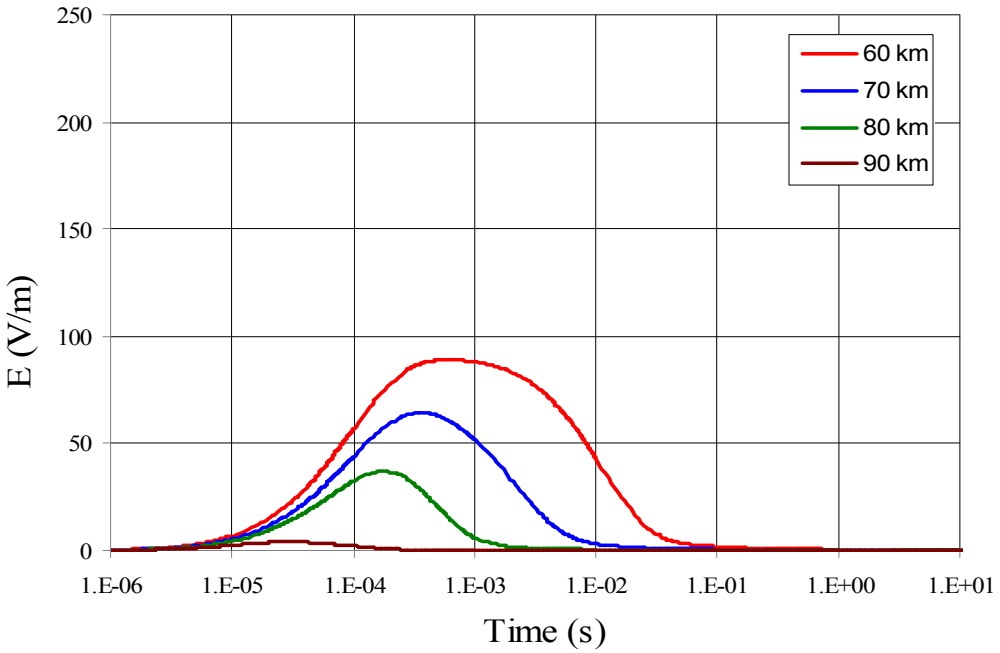

Figure 4.27: Electric field simulations using the non-linear conductivity profile for ρ = 40 km at altitudes of 60-90 km.

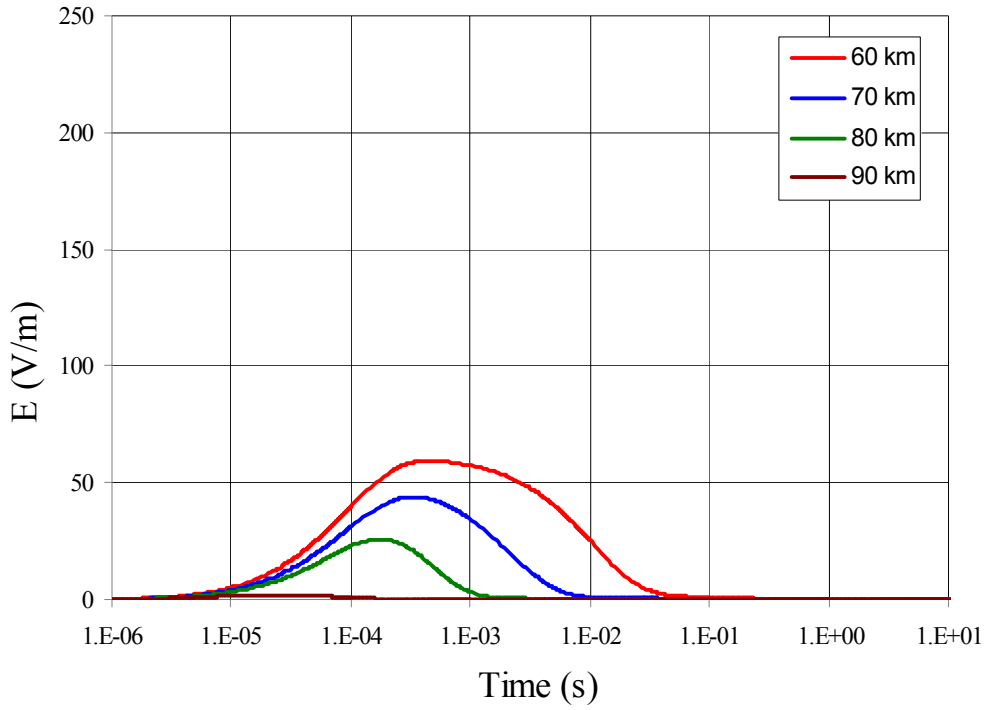

Figure 4.28: Electric field simulations using the non-linear conductivity profile for ρ = 50 km at altitudes of 60-90 km.

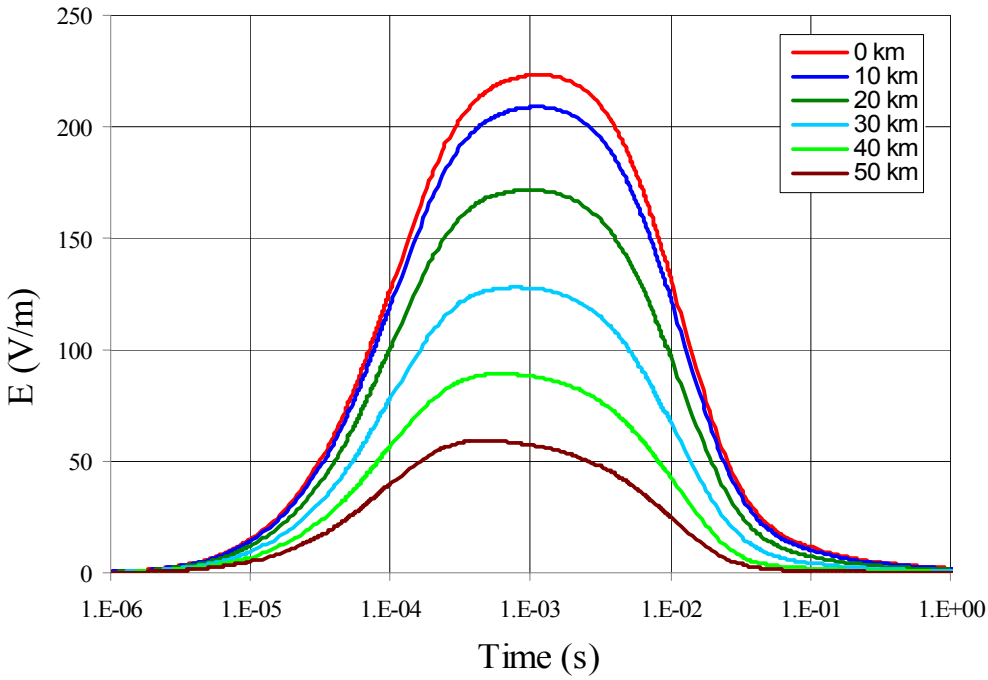

Figure 4.29: Electric field simulations using the non-linear conductivity profile for z = 60 km at radial distances of 0-50 km.

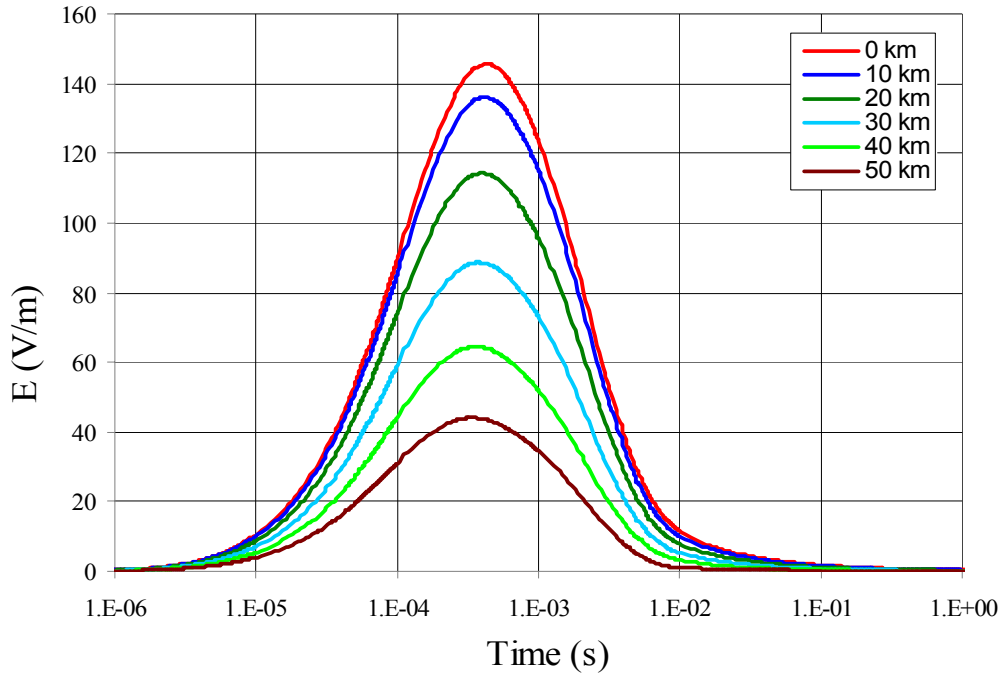

Figure 4.30: Electric field simulations using the non-linear conductivity profile for z = 70 km at radial distances of 0-50 km.

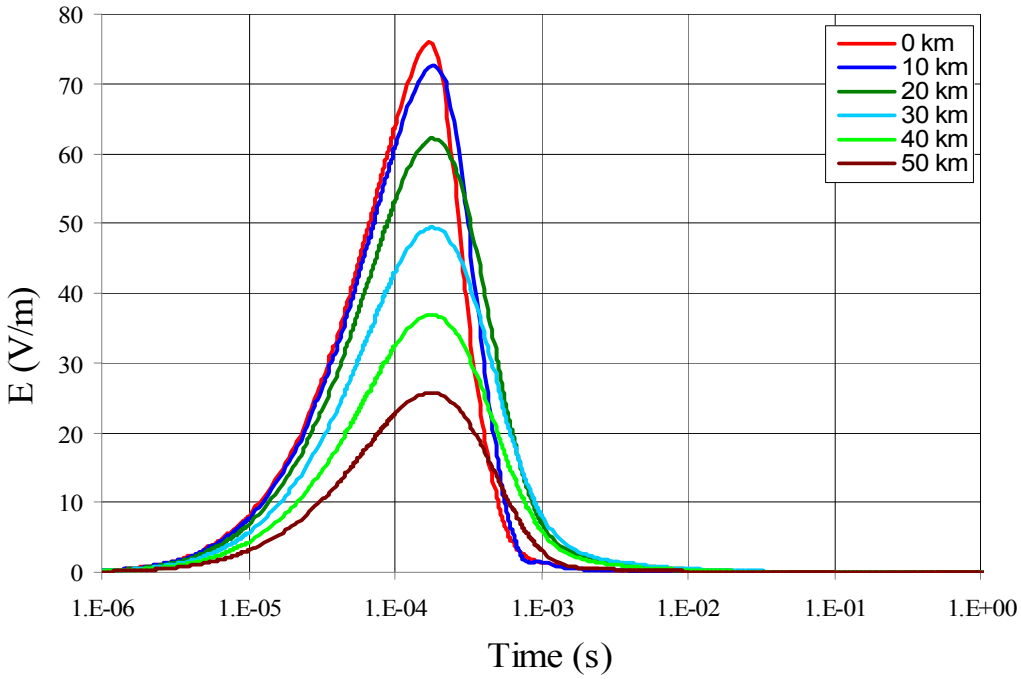

Figure 4.31: Electric field simulations using the non-linear conductivity profile for z = 80 km at radial distances of 0-50 km.

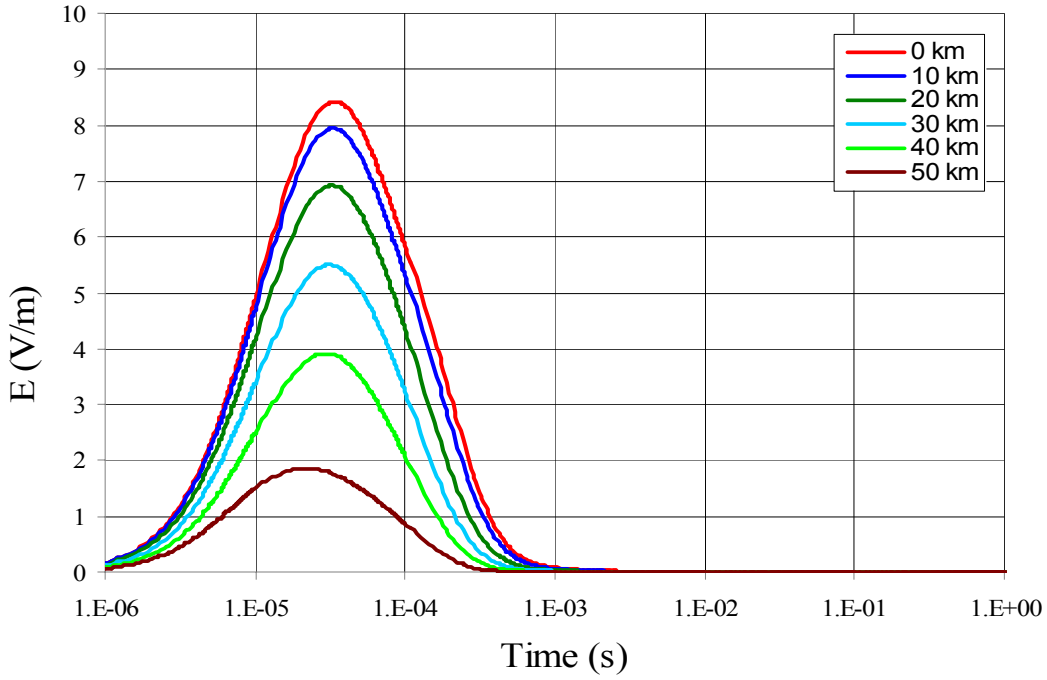

Figure 4.32: Electric field simulations using the non-linear conductivity profile for z = 90 km at radial distances of 0-50 km.

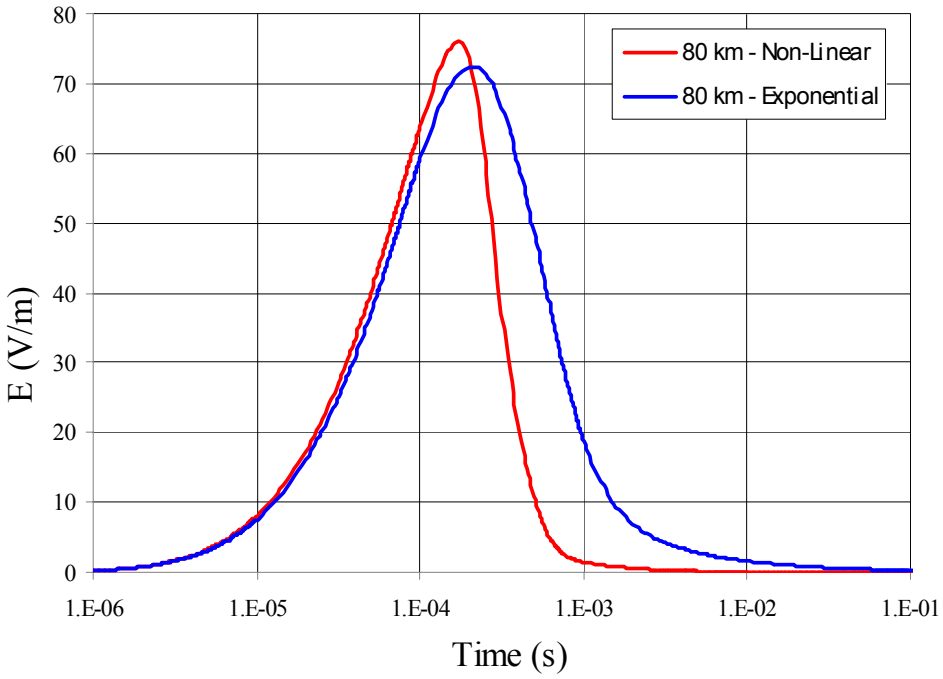

Figure 4.33: Electric field simulations at ρ = 0 km and z = 80 km for the exponential and the non-linear conductivity profiles.

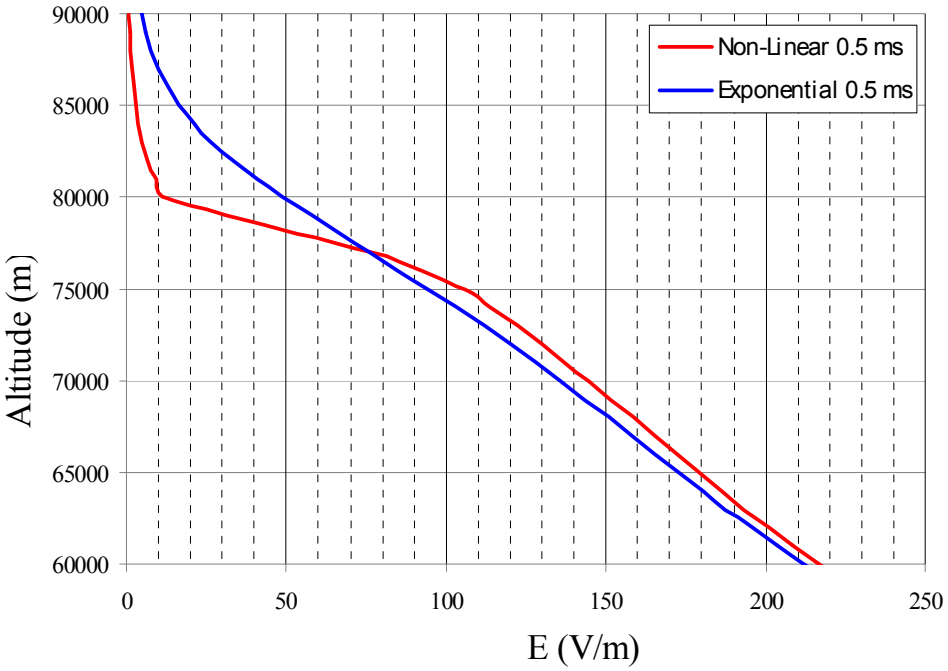

Figure 4.34: Electric field simulations at ρ = 0 km and z = 60-90 km for the exponential and the non-linear conductivity profiles at a time of 0.5 ms.

4.3.2 Vertical and Horizontal Electric Field Results

Figs. 4.35-4.42 show the vertical and horizontal electric fields for the non-linear conductivity simulation. Each of these components is shown at elevations varying from 60-90 km with radial distances ranging from 0-50 km. Observations from these results follow.

1. The electric field is primarily vertically oriented. This trait is seen for the ambient conductivity simulations also.
2. For the vertical electric fields, the maximum peak value occurs on the z-axis (vertical) for all altitudes with the magnitude decreasing as the radial distance increases. For the horizontal electric fields, the maximum peak value occurs at a radial distance of 30-40 km for all cases of interest.

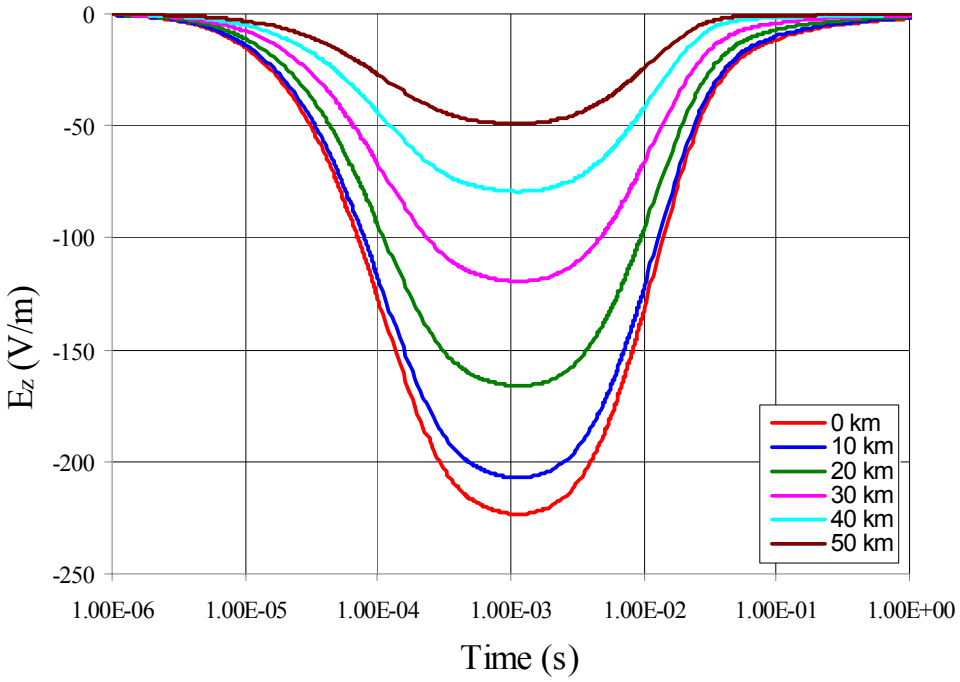

Figure 4.35 Vertical electric field simulations using the non-linear conductivity profile for 60 km altitude at radial distances of 0-50 km.

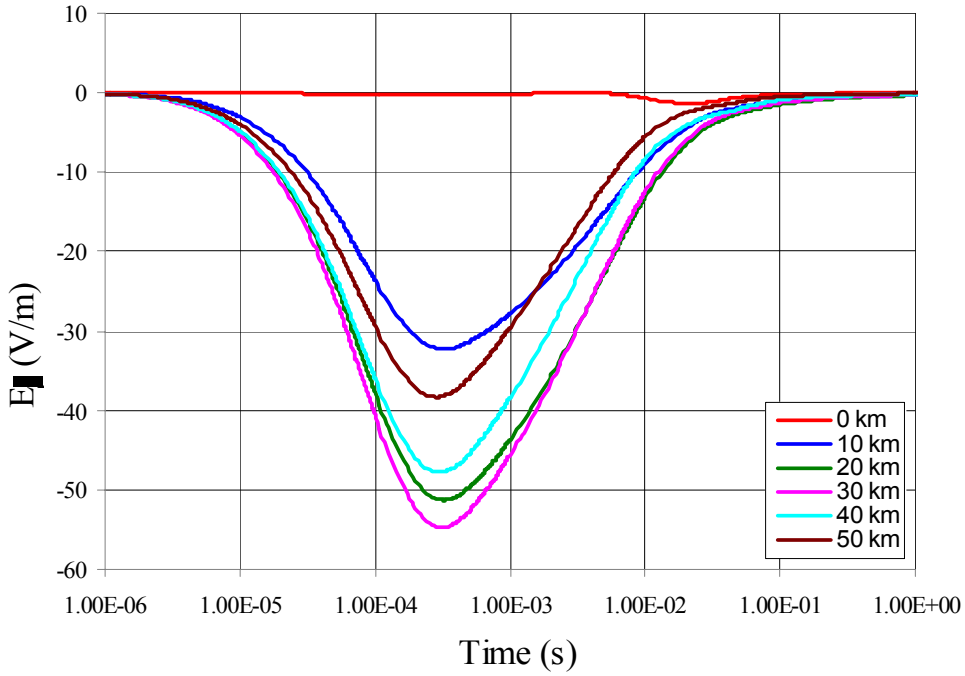

Figure 4.36 Horizontal electric field simulations using the non-linear conductivity profile for 60 km altitude at radial distances of 0-50 km.

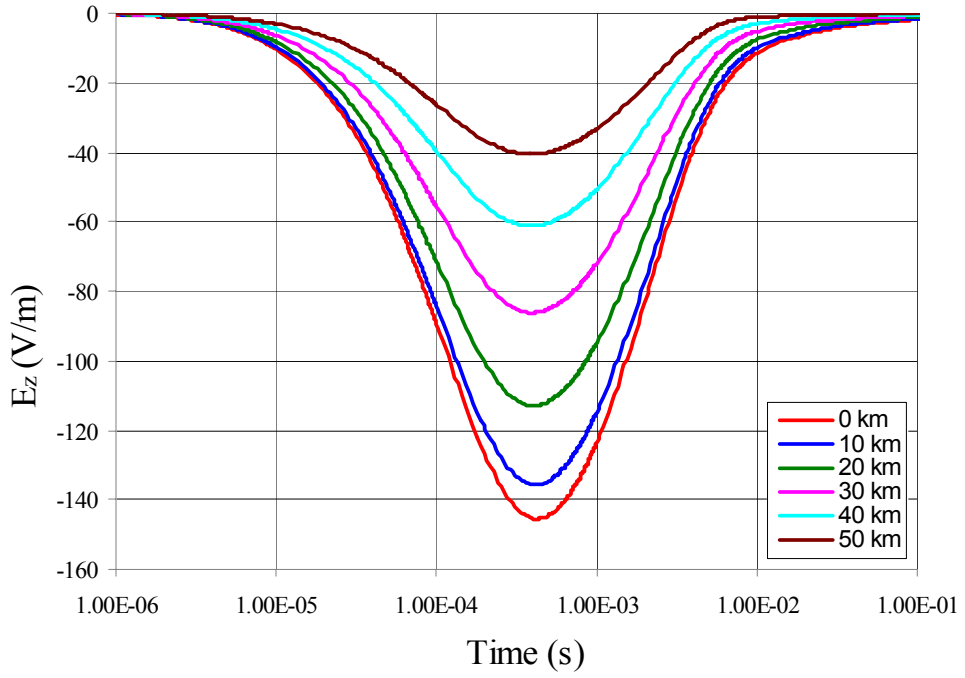

Figure 4.37: Vertical electric field simulations using the non-linear conductivity profile for 70 km altitude at radial distances of 0-50 km.

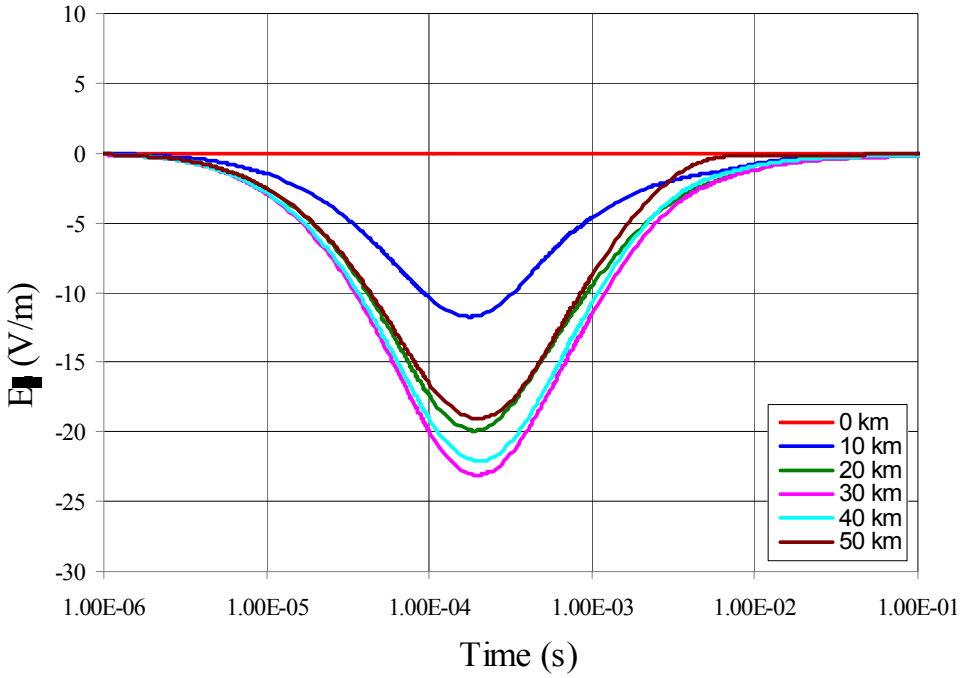

Figure 4.38: Horizontal electric field simulations using the non-linear conductivity profile for 70 km altitude at radial distances of 0-50 km.

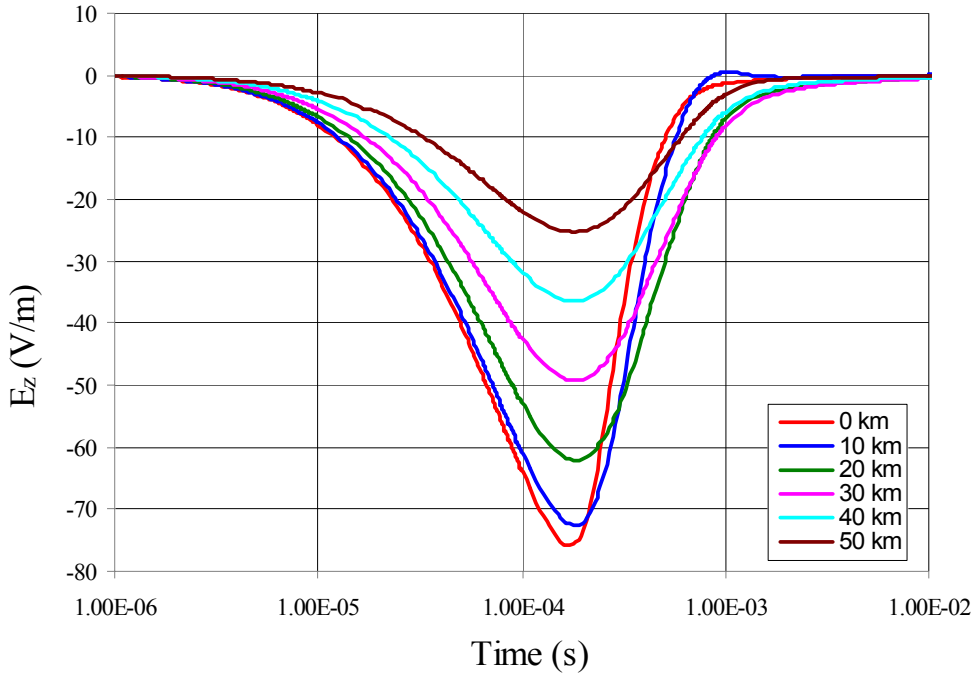

Figure 4.39: Vertical electric field simulations using the non-linear conductivity profile for 80 km altitude at radial distances of 0-50 km.

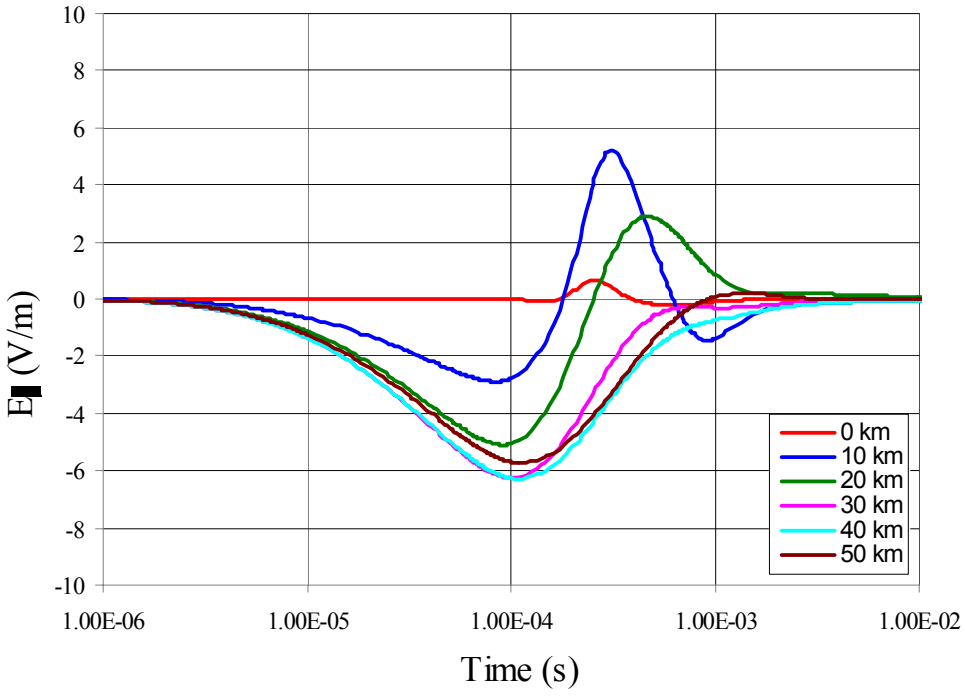

Figure 4.40: Horizontal electric field simulations using the non-linear conductivity profile for 80 km altitude at radial distances of 0-50 km.

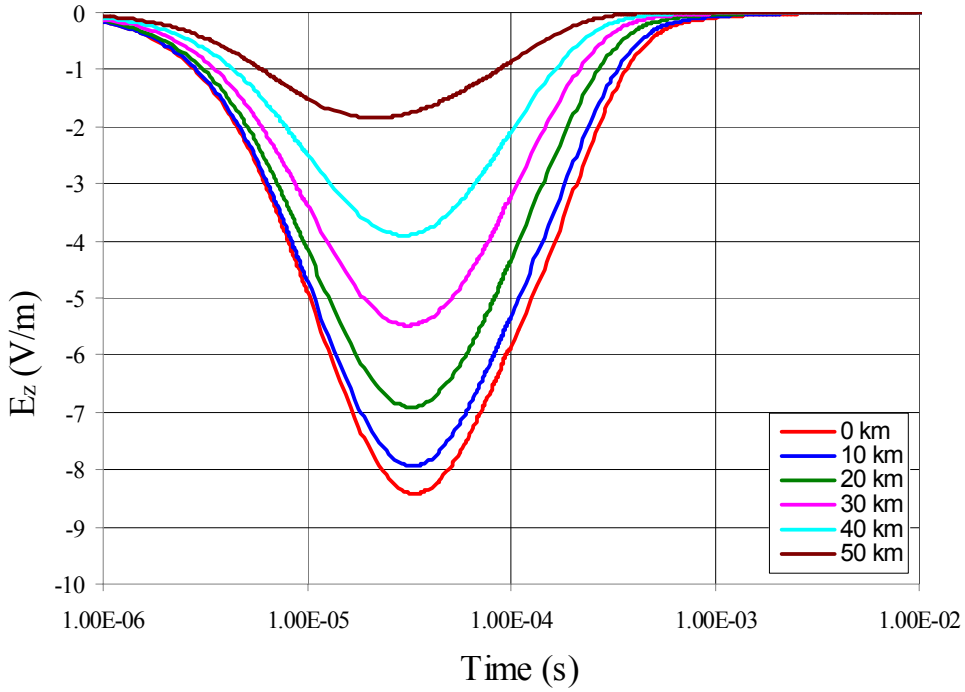

Figure 4.41: Vertical electric field simulations using the non-linear conductivity profile for 90 km altitude at radial distances of 0-50 km.

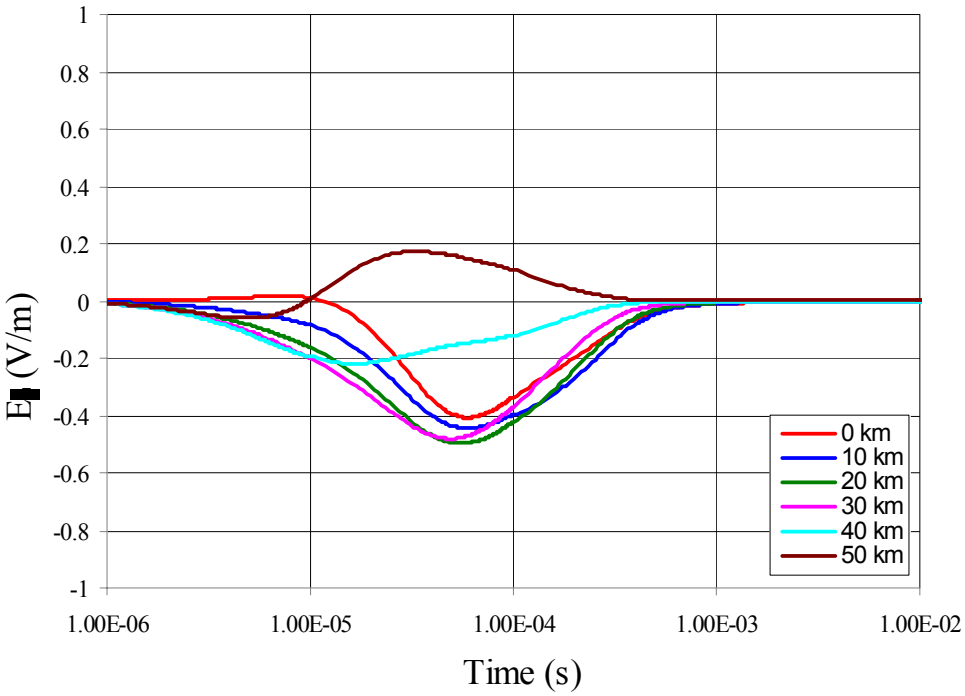

Figure 4.42: Horizontal electric field simulations using the non-linear conductivity profile for 90 km altitude at radial distances of 0-50 km.

4.3.3 Conductivity and Electron Density Results

This section discusses the behavior of the non-linear conductivity used in the simulation. According to Eqns. (2.12) and (2.15), the total conductivity is given by $\sigma = \sigma_i + q_e N_e \mu_e$ where σ_i is the ambient ion exponential model, μ_e, the electron mobility, and N_e, the electron number density.

Fig. 4.43 shows the simulated electric fields for altitudes from 60-90 km at radial distances varying from 0-50 km compared to the characteristic breakdown field. The electric field values shown are calculated to be the maximum values at each location over the entire time span of the simulation. The region in altitude and radial distance corresponding to the electric field values greater than the breakdown field is where ionization occurs. This results in photon emissions in the optical band, identifying the presence of a sprite [7, 36, 37].

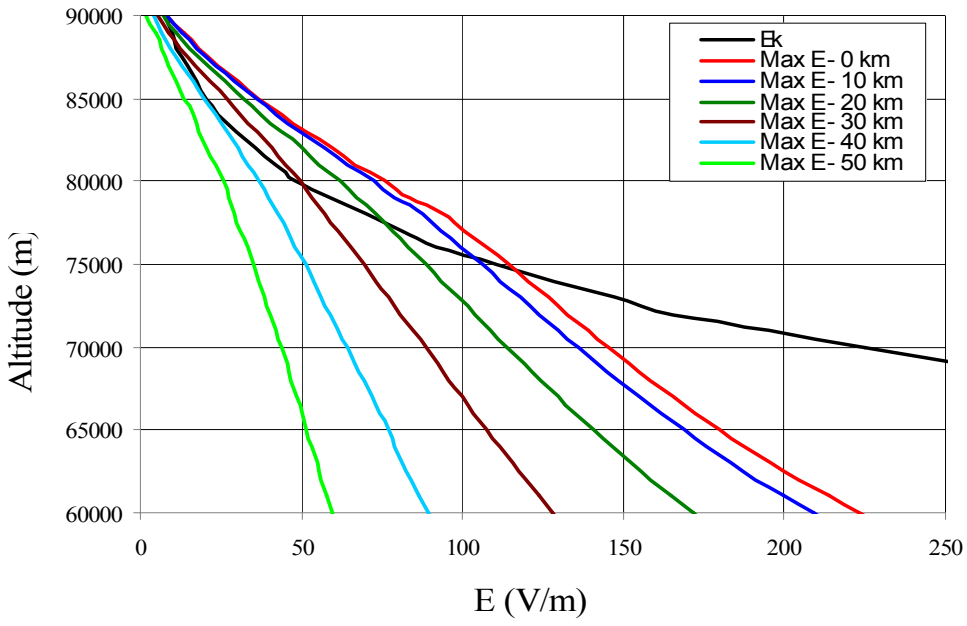

Figure 4.43: Maximum electric field strengths over time for altitudes from 60-90 km at radial distances from 0-50 km compared to the characteristic air breakdown field.

Figs. 4.44 and 4.45 show the conductivity profiles for altitudes from 60-95 km at radial distances varying from 0-30 km for 1 and 100 ms times. Figs. 4.46-4.47 show the corresponding electron number densities. The ambient profiles have been added to the four plots for comparison. The electron densities computed in this simulation are confirmed by the results of earlier work shown by Fig. 4.48 [37]. These results show the electron density changes for three ambient electron density models [37]. While greater change is shown in the earlier work, a much larger total charge was also used.

The remaining figures are broken up into groups of four at different altitudes. Figs. 4.49-52 are at 60 km, Figs. 4.53-56 at 70 km, Figs. 4.57-60 at 80 km, and Figs. 4.61-64 at 90 km. In each group, the first plot is the conductivity, second is the electron mobility, third is the number density of electrons, and last is the difference between the ionization and attachment coefficients. Each plot presents results for the simulations at radial distances from 0-50 km. The following are some observations and explanations of these results.

1. The change in conductivity due to the electric field increased with altitude. This is a direct result of the level of ionization increasing as altitude is increased. At 60 km, the conductivity changes by less than one percent while at 90 km, it changes by over an order of magnitude.
2. At a given altitude, the temporal behavior of the conductivity tends to track the behavior of the electron mobility.
3. The value for the electron number density after the transient slightly differs from the ambient values for the cases shown. If the electric fields do not reach the

characteristic breakdown field, ν_i - ν_a stays negative and therefore the final value of the electron number density will be slightly less than the ambient value. Likewise, when the electric field exceeds the breakdown field, the number density will increase for that period of time. This is a second order effect that is due to the omission of the αN_e^2 term, discussed in Section 2.4.2.3, from the electron ionization equation. However, the inclusion of this term makes the solution very numerically intensive. Additionally, the value is not well known for high altitudes.

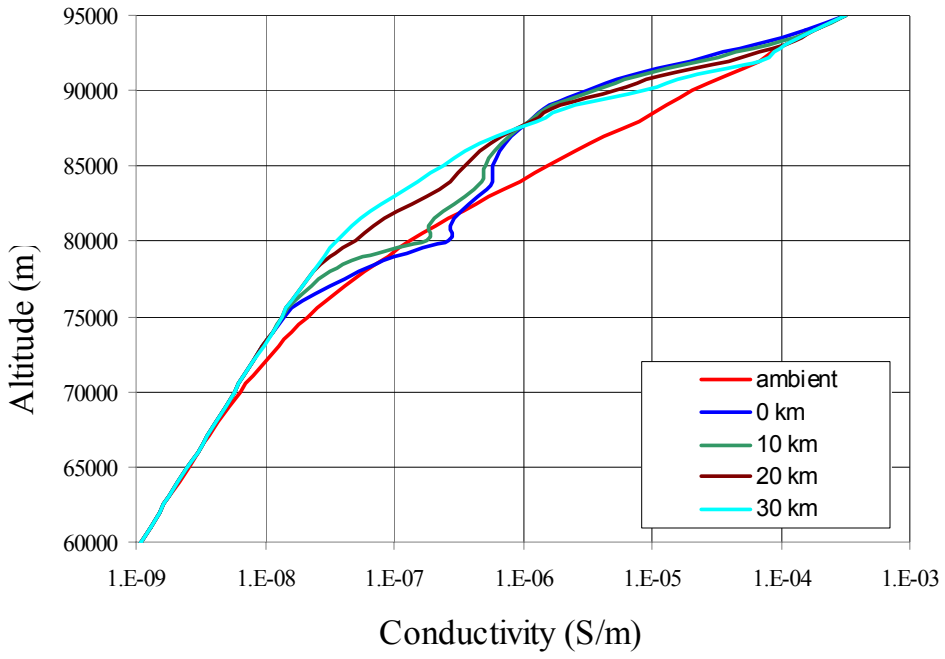

Figure 4.44: Conductivity profiles using the non-linear model at 1 ms for radial distances from 0-30 km. The ambient profile is shown for reference.

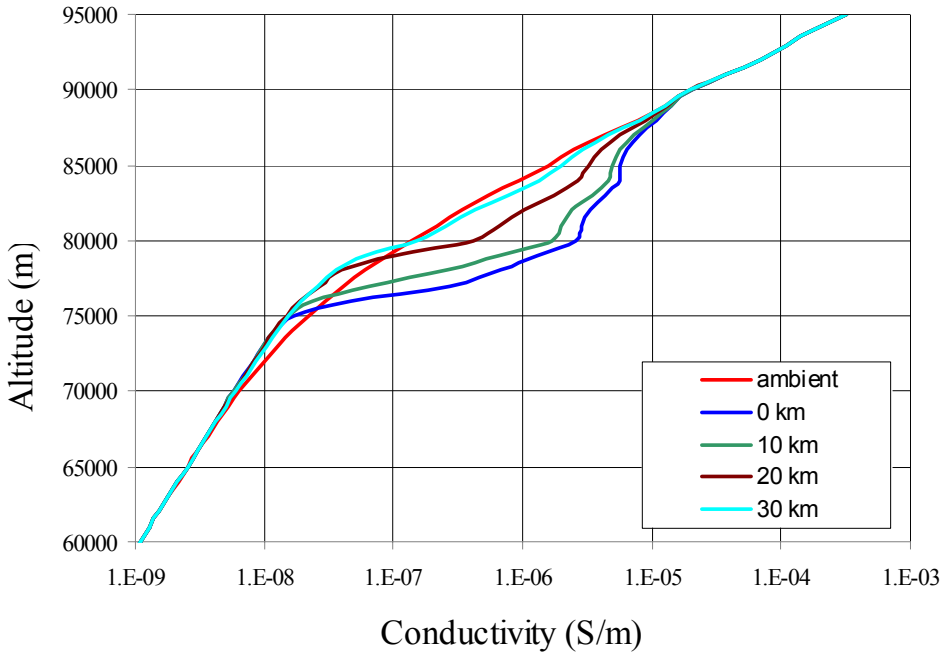

Figure 4.45: Conductivity profiles using the non-linear model at 100 ms for radial distances from 0-30 km. The ambient profile is shown for reference.

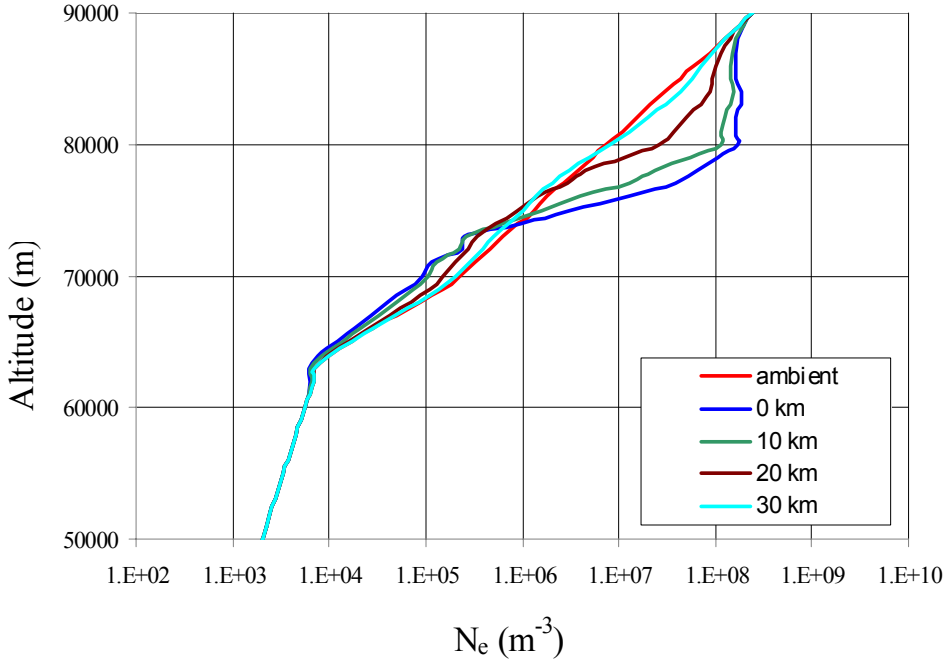

Figure 4.46: Electron density profiles using the non-linear conductivity model at 1 ms for radial distances from 0-30 km. The ambient profile is shown for reference.

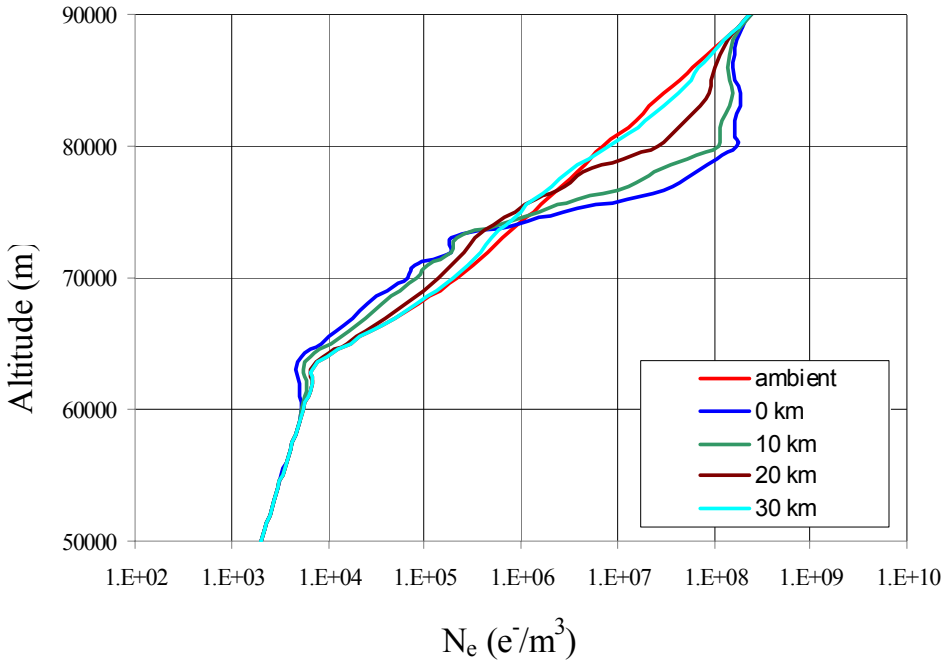

Figure 4.47: Electron density profiles using the non-linear conductivity model at 100 ms for radial distances from 0-30 km. The ambient profile is shown for reference.

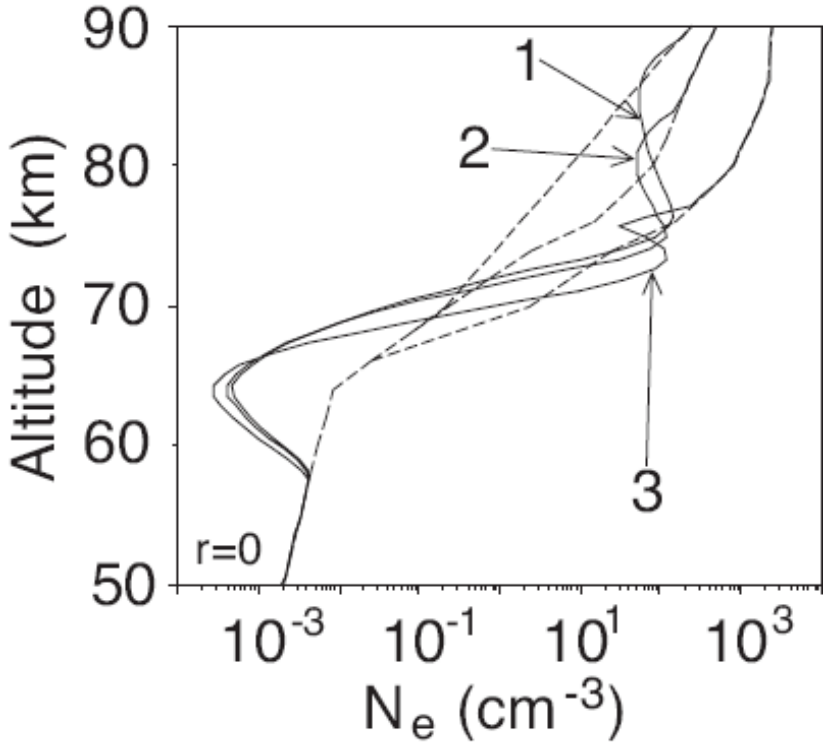

Figure 4.48: Electron density changes corresponding to three ambient electron density models for 200 C CG stroke, provided by Dr. V. P. Pasko [37].

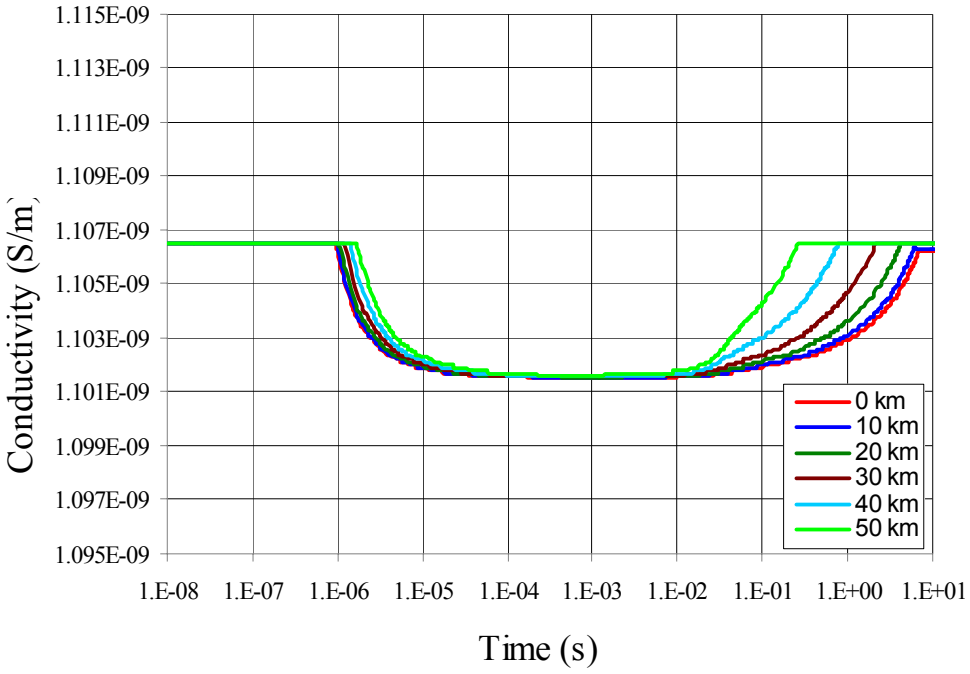

Figure 4.49: Conductivity profile using the non-linear model at 60 km altitude for radial distances from 0-50 km.

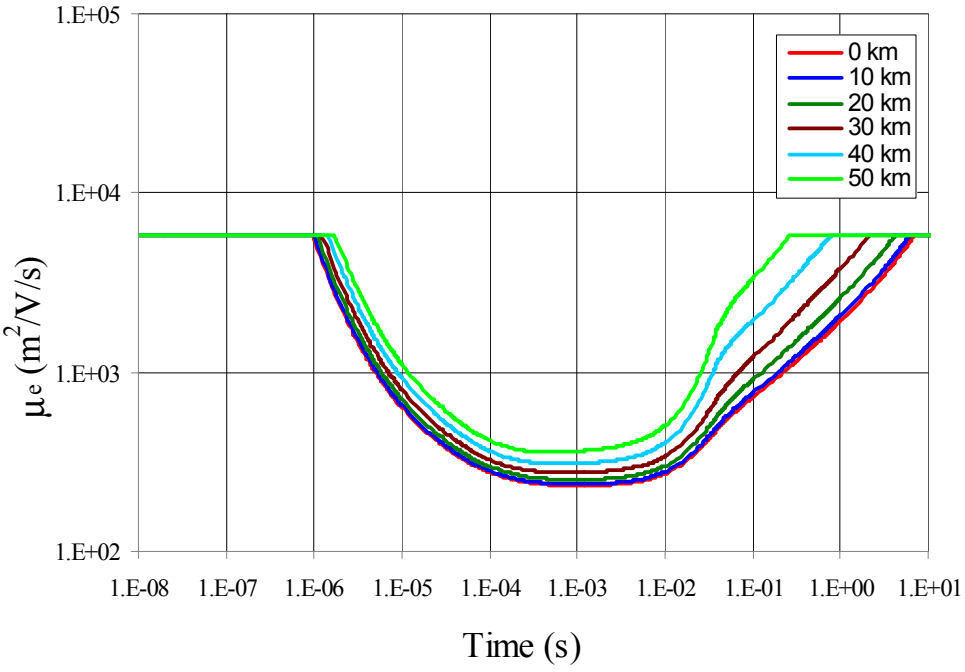

Figure 4.50: Electron mobility using the non-linear conductivity model at 60 km altitude for radial distances from 0-50 km.

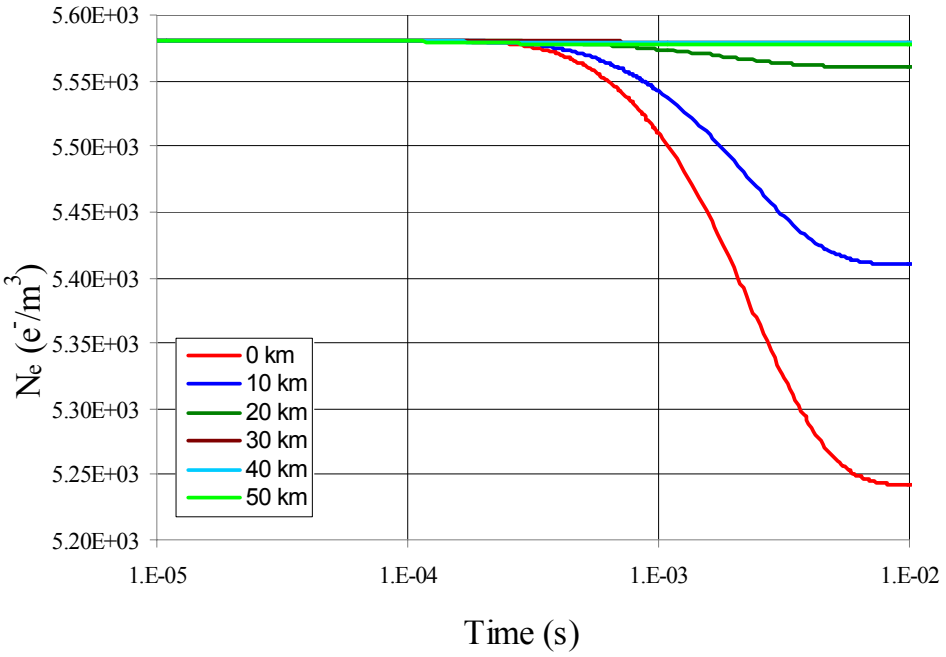

Figure 4.51: Electron number density using the non-linear conductivity model at 60 km altitude for radial distances from 0-50 km.

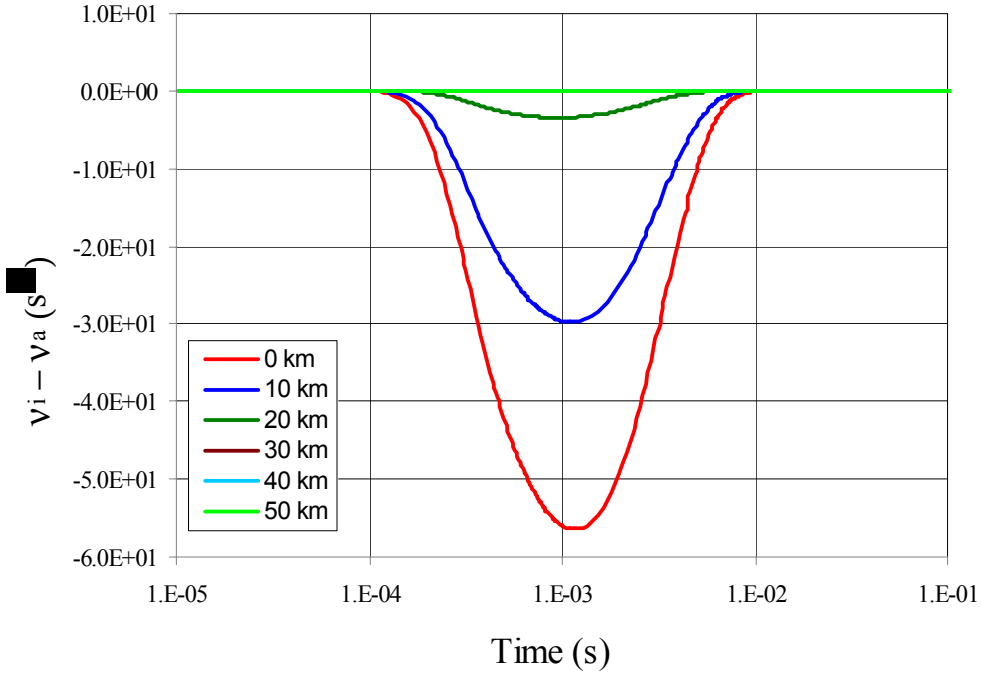

Figure 4.52: Difference between ionization and attachment coefficients, ν_i - ν_a, using the non-linear conductivity model at 60 km altitude for radial distances from 0-50 km.

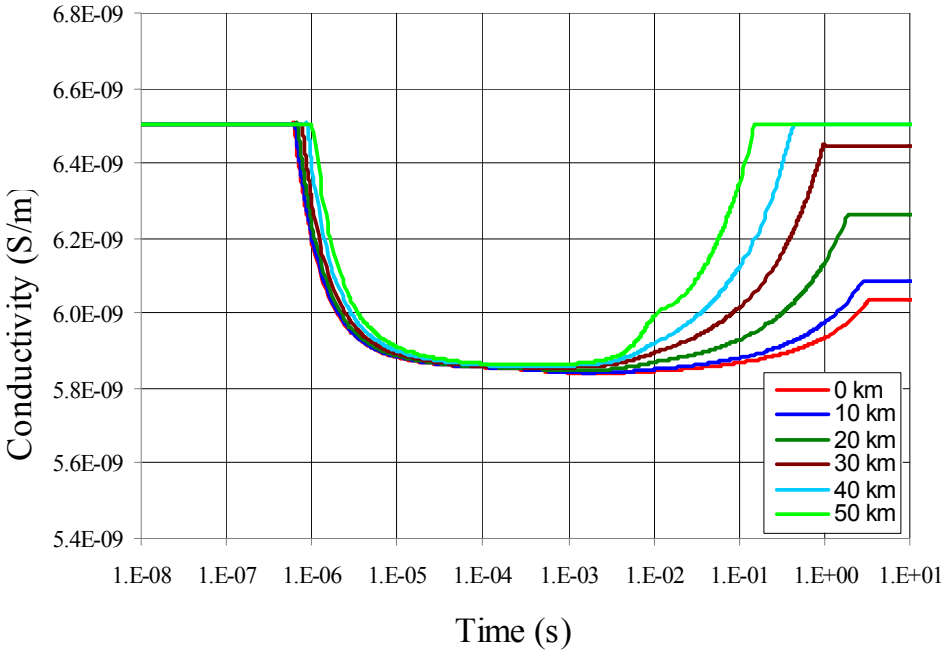

Figure 4.53: Conductivity profile using the non-linear model at 70 km altitude for radial distances from 0-50 km.

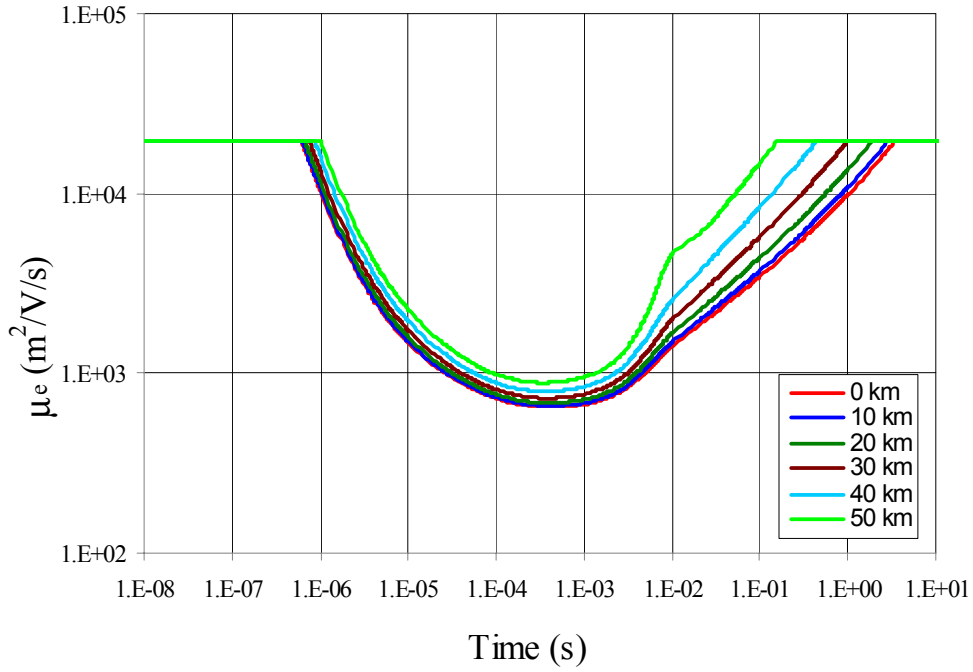

Figure 4.54: Electron mobility using the non-linear conductivity model at 70 km altitude for radial distances from 0-50 km.

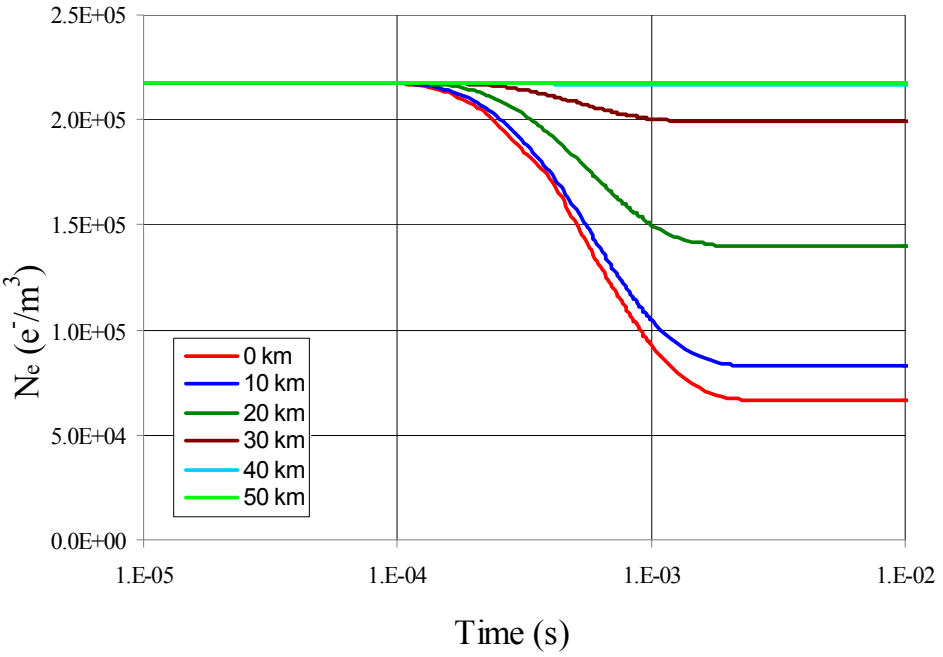

Figure 4.55: Electron number density using the non-linear conductivity model at 70 km altitude for radial distances from 0-50 km.

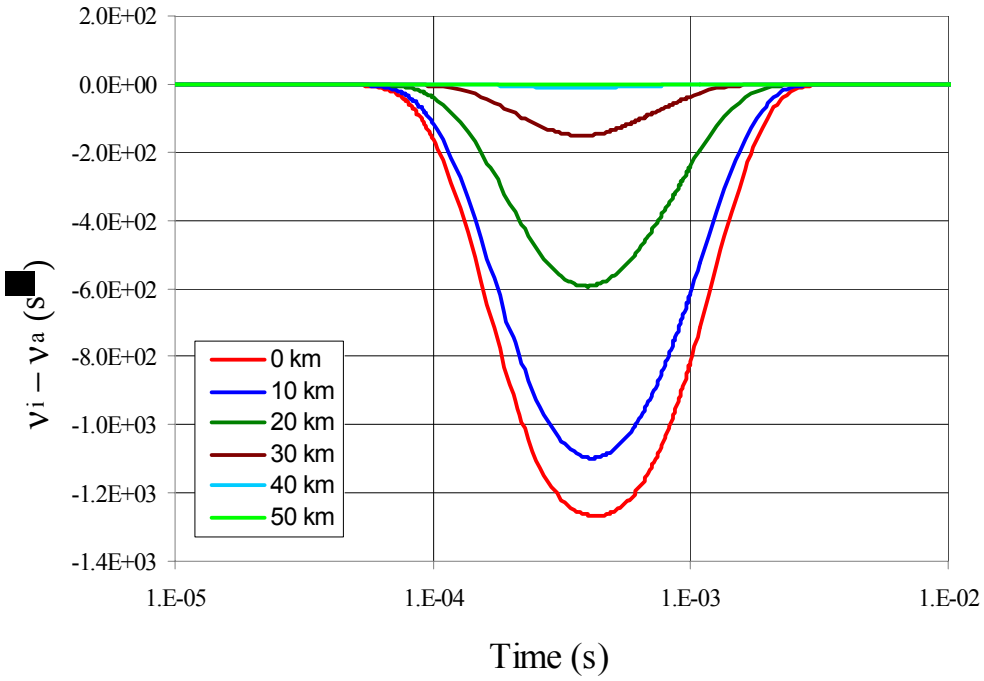

Figure 4.56: Difference between ionization and attachment coefficients, ν_i - ν_a, using the non-linear conductivity model at 70 km altitude for radial distances from 0-50 km.

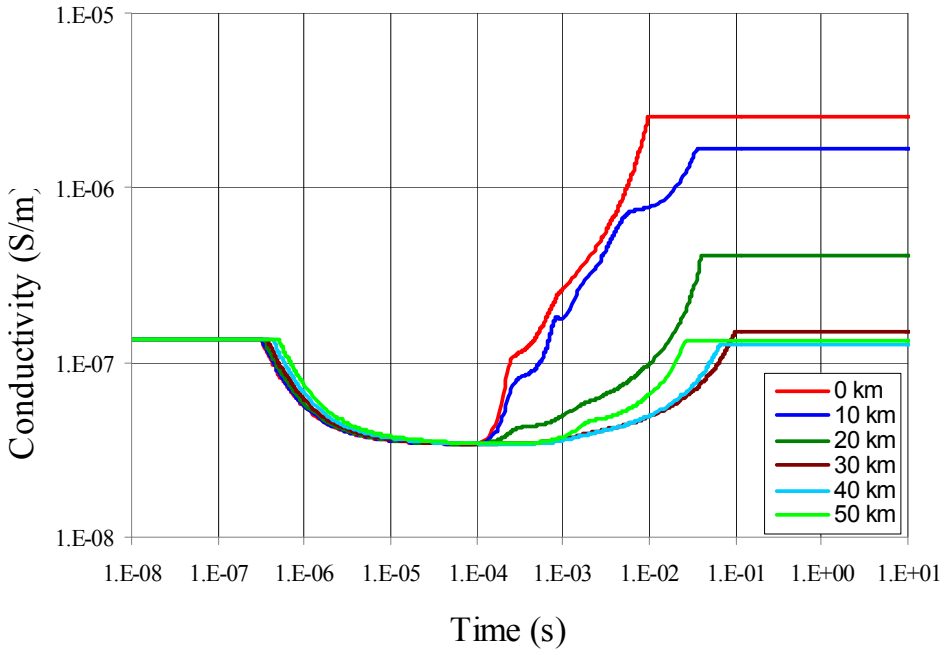

Figure 4.57: Conductivity profile using the non-linear model at 80 km altitude for radial distances from 0-50 km.

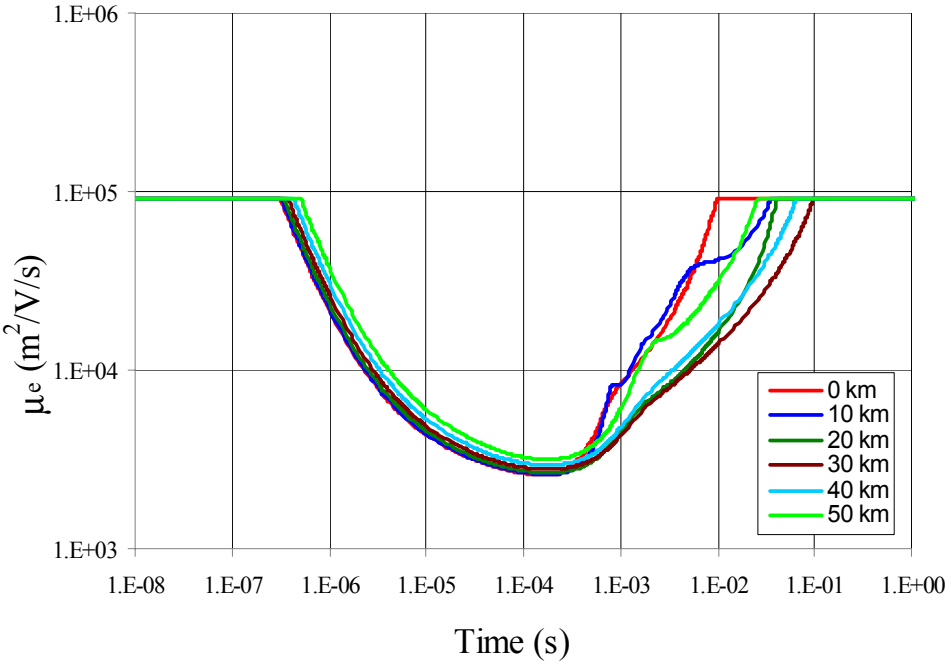

Figure 4.58: Electron mobility using the non-linear conductivity model at 80 km altitude for radial distances from 0-50 km.

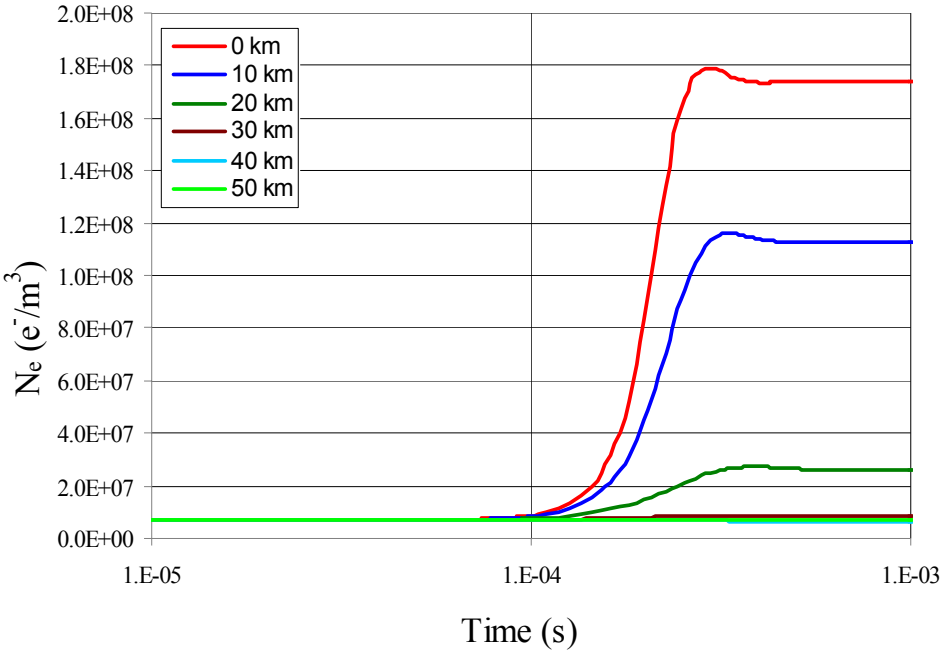

Figure 4.59: Electron number density using the non-linear conductivity model at 80 km altitude for radial distances from 0-50 km.

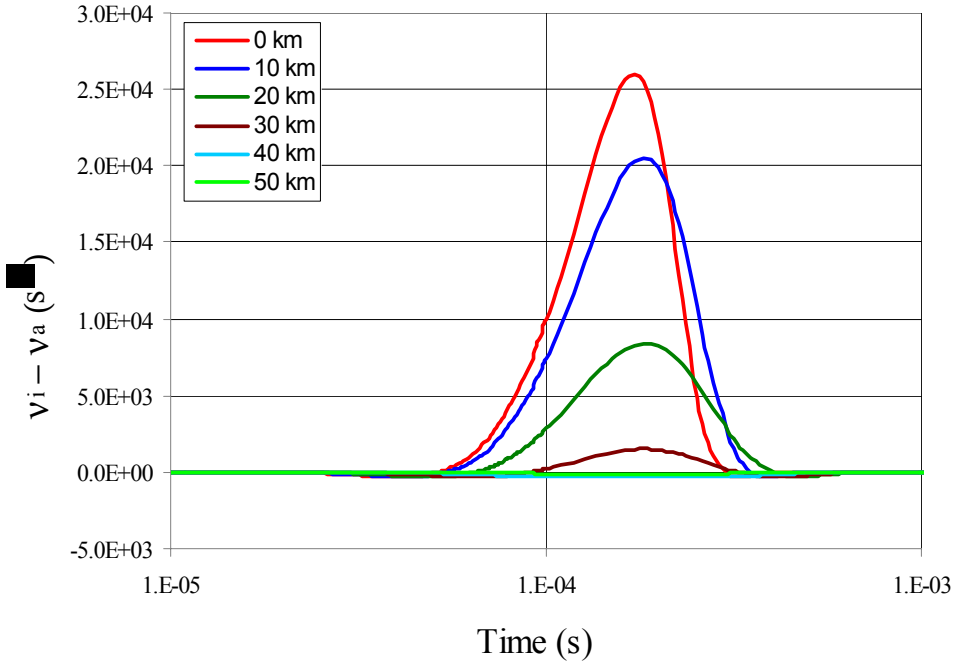

Figure 4.60: Difference between ionization and attachment coefficients, ν_i - ν_a, using the non-linear conductivity model at 80 km altitude for radial distances from 0-50 km.

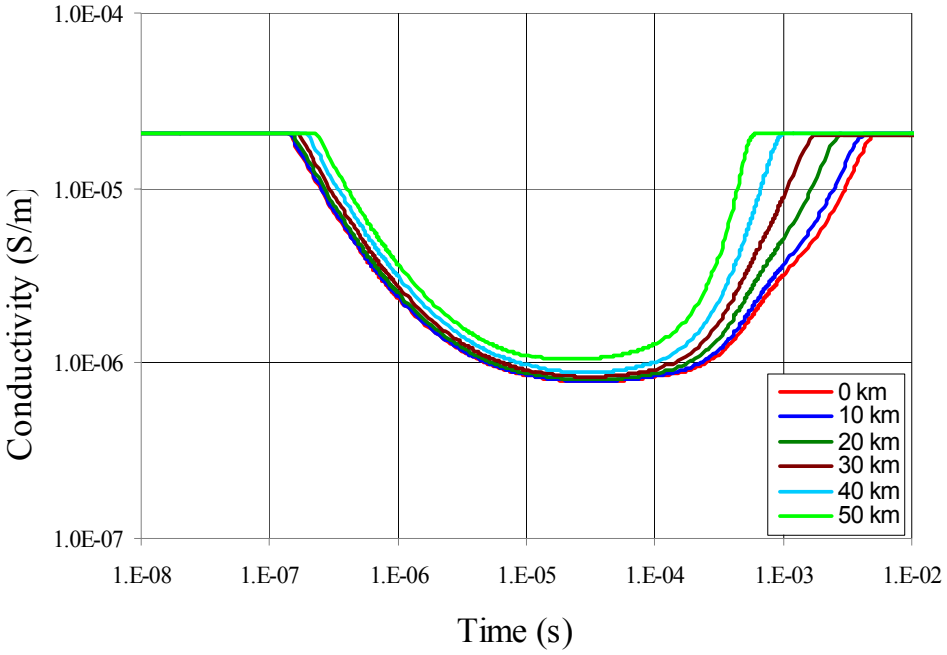

Figure 4.61: Conductivity profile using the non-linear model at 90 km altitude for radial distances from 0-50 km.

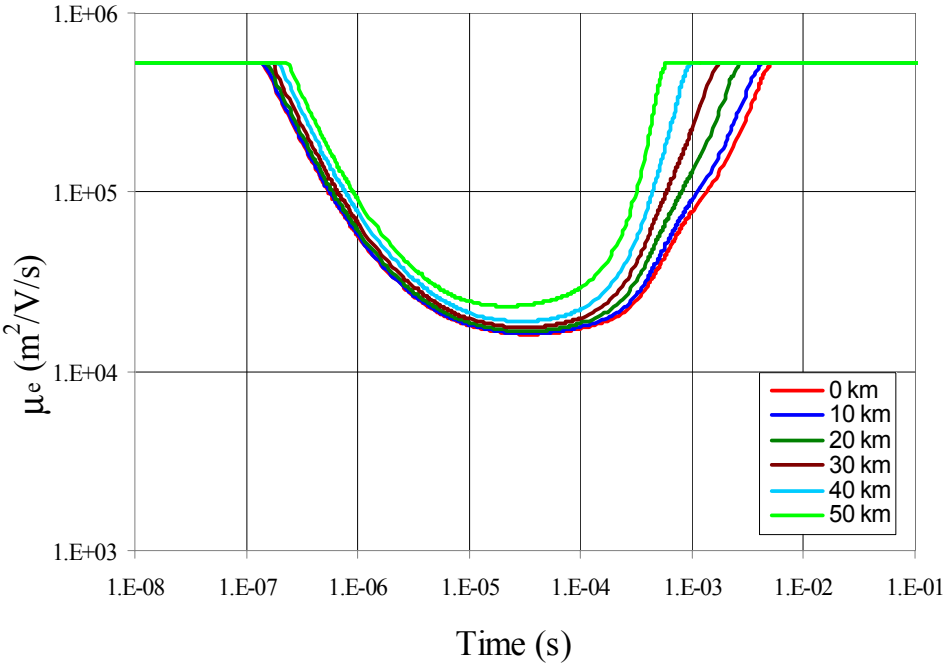

Figure 4.62: Electron mobility using the non-linear conductivity model at 90 km altitude for radial distances from 0-50 km.

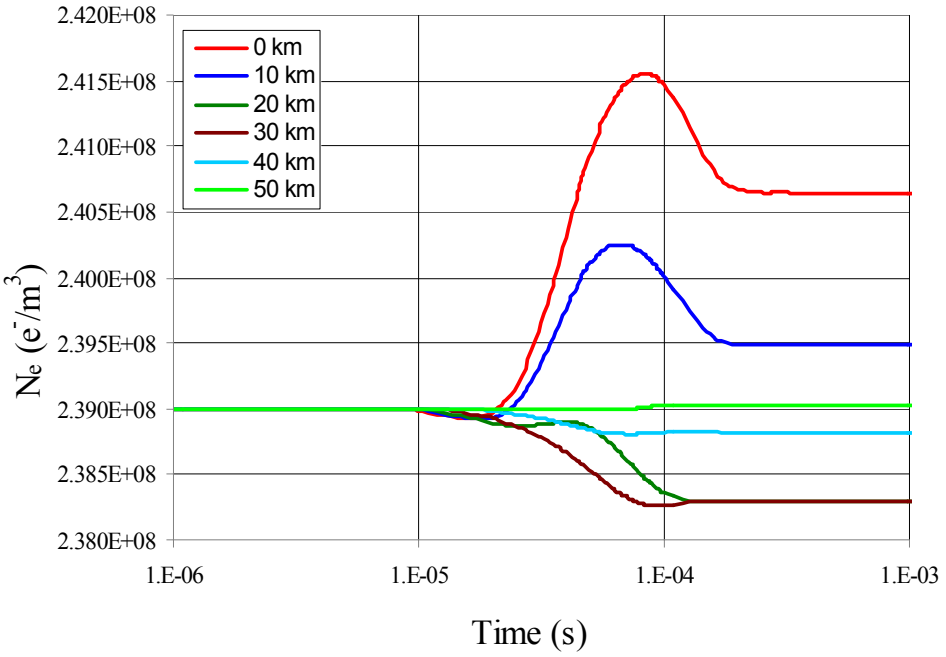

Figure 4.63: Electron number density using the non-linear conductivity model at 90 km altitude for radial distances from 0-50 km.

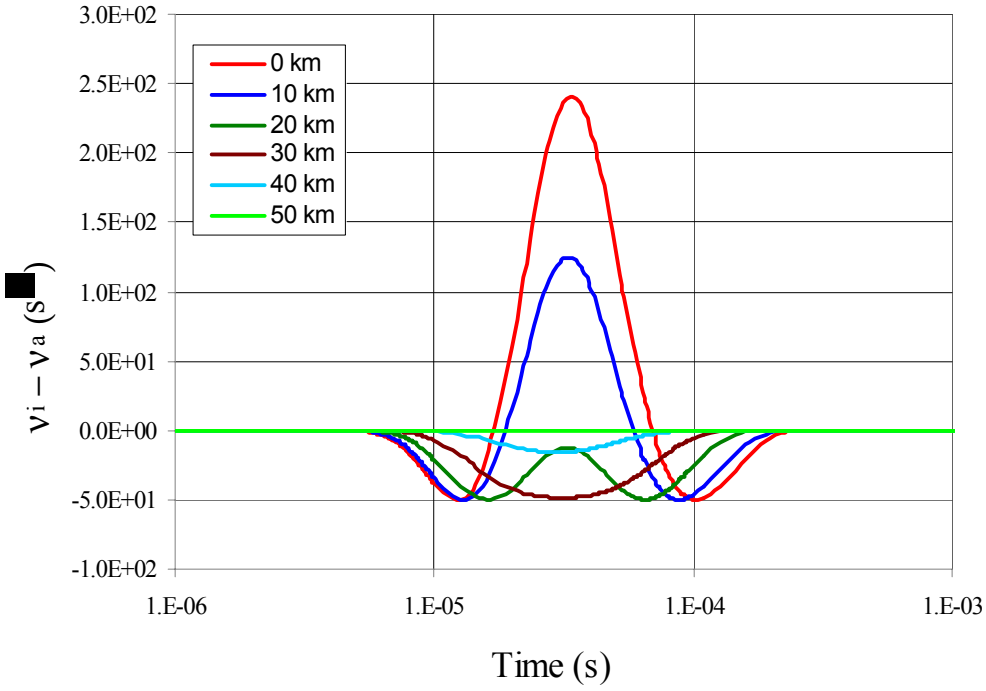

Figure 4.64: Difference between ionization and attachment coefficients, ν_i - ν_a, using the non-linear conductivity model at 90 km altitude for radial distances from 0-50 km.

CHAPTER 5

CONCLUSIONS

This thesis presented simulations using a Finite Element Model with multiple conductivity profiles to add to this body of research to confirm the possibility of a high level of ionization and therefore the presence of a sprite.

In Chapter 3, a Finite Element Model was described that effectively models transient electric field behavior in the atmosphere. These equations are simultaneously solved as opposed to an earlier derivative approach [36, 37, 40].

In Chapter 4, simulations of the transient electric field are presented for a variety of conductivities. The research showed that the upper atmosphere is strongly affected by the quasi-static effects of a positive CG stroke. For the ambient profiles, the electric field reaches its peak value in a matter of milliseconds, and then slowly decays over time. The results agree well with simulations done by Baginski et al. [35, 45, 46, 50]. It was shown at high altitudes the maximum electric field strength decreased in magnitude and occurred at shorter times. When non-linear effects were included in the conductivity, an increase of up to two orders of magnitude in the overall conductivity was observed. At 90 km altitude, this effectively "shorted out" the electric field.

Results for the non-linear conductivity profile were then presented. The electron component of the conductivity does not modify the results at altitudes below 60 km [37, 52]. At higher altitudes, the electric field results had differences compared to the ambient

conductivity models. A sharp increased rate of decay in electric field strength at 80 km was observed. Fig. 4.43 show the region of the simulation where ionization occurred, identifying the presence of a sprite.

Figs. 4.46 and 4.47 show the electron density profiles with respect to the ambient values at two time periods. These figures confirmed the results of the simulation when compared to previous work shown by Fig. 4.48 [37]. While the earlier work showed a greater divergence from the ambient values, [37] used a much larger total. At 80 km altitude, the electron density reached values over an order of magnitude greater than the ambient. This led to an increase in the conductivity which directly resulted in the sharp decrease of the electric field strength.

5.1 Future Work

The research presented here suggests future research should focus on possible inclusion of the αN_e^2 term to the model. Ideally all the transient conductivities should return to the ambient values. A denser mesh can be added to the region where the sprite is expected to occur. Visual evidence shows, sprites are similar to individual columns with diameters on the order of just a few kilometers [14, 17, 18] suggesting a more discretized model be used in the vicinity of the sprite.

BIBLIOGRAPHY

[1] R. C. Franz, R. J. Nemzek, and J. R. Winckler, "Television image of a large upward electrical discharge above a thunderstorm system," *Science*, vol. 249, no. 4964, pp. 48-51, July 1990.

[2] D. D. Sentman and E. M. Wescott, "Red sprites and blue jets: Thunderstorm-excited optical emissions in the stratosphere, mesosphere, and ionosphere," *Phys. Plasmas*, vol. 2, no. 6, pp 2514-2522, June 1995.

[3] V. P. Pasko, U. S. Inan, and T. F. Bell, "Sprites as evidence of vertical gravity wave structures above mesoscale thunderstorms," *Geophysical Research Letters*, vol. 24, no. 14, pp. 1735-1738, July 1997.

[4] S. B. Mende and D. D. Sentman, "Lightning between earth and space," *Scientific American*, vol. 277, iss. 2, pp. 56-59, Aug. 1997.

[5] H. C. Stenbaek-Nielsen, D. R. Moudry, E. M. Wescott, D. D. Sentman, and F. T. Sâo Sabbas, "Sprites and Possible Mesospheric Effects," *Geophysical Research Letters*, vol. 27, no. 23, pp. 3829-3832, Dec. 2000.

[6] L. Tong, Y. Hiraki, K. Nanbu, and H. Fukunishi, "Release of positive charges producing sprite halos," *Journal of Atmospheric and Solar-Terrestrial Physics*, 65, pp 829-838, 2005.

[7] E. R. Williams, "Sprites, elves, and glow discharge tubes," *Physics Today*, vol. 54, issue 22, pp. 41-49, Nov. 2001.

[8] M. Stanley, M. Brook, P. Krehbiel, and S. A. Cummer, "Detection of daytime sprites via a unique sprite ELF signature," *Geophysical Research Letters*, vol. 27, no. 6, pp. 871-874, Mar. 2000.

[9] C. P. Barrington-Leigh and U. S. Inan, "Elves triggered by positive and negative lightning," *Geophysical Research Letters*, vol. 26, no. 6, pp. 683-686, March 1999.

[10] Y. Hobara, N. Iwasaki, T. Hayashida, M. Hayakawa, K. Ohta, and H. Fukunishi, "Interrelation between ELF transients and ionospheric disturbances in association

with sprites and elves," *Geophysical Research Letters*, vol. 28, no. 5, pp. 935-938, March 2001.

[11] U. S. Inan, J. V. Rodriguez, and V. P. Idone, "VLF signatures of lightning-induced heating and ionization of the nighttime d-region," *Geophysical Research Letters*, vol. 20, no. 21, pp. 2355-2358, Nov. 1993.

[12] Y. P. Raizer, G. M. Milikh, M. N. Shneider, and S. V. Novakovski, "Long streamers in the upper atmosphere above thundercloud," *Journal of Physics D: Applied Physics*, vol. 31, no. 22, pp. 3255-3264, Nov. 1998.

[13] V. P. Pasko and H. C. Stenbaek-Nielsen, "Diffuse and streamer regions of sprites," *Geophysical Research Letters*, vol. 29, no. 10, 10.1029/2001GL014241, 2002.

[14] U. S. Inan, "Lightning effects at high altitudes: sprites, elves, and terrestrial gamma ray flashes," *Applied Physics*, S1631-0705, pp. 1411-1421, 2002.

[15] N. Liu and V. P. Pasko, "Molecular nitrogen LBH band system far-UV emissions of sprite streamers," *Geophysical Research Letters*, vol. 32, L05104, doi:10.1029/2004GL022001, 2005.

[16] M. Stanley, P. Krehbiel, M. Brook, C. Moore, W. Rison, and B. Abrahams, "High speed video of initial sprite development," *Geophysical Research Letters*, vol. 26, no. 20, pp. 3201-3204, 1999.

[17] S. F. Hardman, C. J. Roger, R. L. Dowden, and J. B. Brundell, "Measurements of the VLF scattering pattern of the structured plasma of red sprites," *IEEE Antennas and Propagation Magazine*, vol. 40, no. 2, pp. 29-38, Apr. 1998.

[18] C. J. Rodger, J. R. Wait, and N. R. Thomson, "VLF scattering from red sprites: vertical columns of ionisation in the earth-ionosphere waveguide," *Proceedings from the VIIth International Conference on Mathematical Methods in Electromagnetic Theory*, Kharkov, Ukraine, pp 282-284, 1998.

[19] V. P. Pasko, M. A. Stanley, J. D. Matthews, U. S. Inan, and T. G. Wood, "Electrical discharge from a thundercloud top to the lower ionosphere," *Letters to Nature*, vol. 416, pp. 152-154, March 2002.

[20] W. A. Lyons, T. E. Nelson, R. A. Armstrong, V. P. Pasko, and M. A. Stanley, "Upward electrical discharges from thunderstorm tops," *Bulletin of the American Meteorological Society*, vol. 84, issue 4, pp. 445-454, April 2003.

[21] R. Dowden, J. Brundell, C. Rodger, O. Mochanov, W. Lyons, and T. Nelson, "The structure of red sprites determined by VLF scattering," *IEEE Antennas and Propagation Magazine*, vol. 38, no. 3, pp. 7-15, June 1996.

[22] V. P. Pasko, "Electric jets," *Nature*, vol. 423, pp. 927-929, June 2003.

[23] T. A. Seliga, J. D. Sahr, and R. H. Holzworth, "Probing electric fields near sprites and jets using multiparameter radar and chaff," *IGARSS 1996. 1996 International Geoscience and Remote Sensing Symposium. Remote Sensing for a Sustainable Future*, vol. 1, pp 569-573, May 1996.

[24] E. A. Bering III, J. R. Benbrook, J. A. Garrett, A. M. Parades, E. M. Wescott, D. R. Moudry, D. D. Sentman, H. C. Stenbaek-Nielson, and W. A. Lyons, "Sprite and Elve Electrodynamics," *Advances in Space Research*, vol. 30, no. 11, pp. 2585-2595, 2002.

[25] D. Moudry, H. Stenbaek-Nielsen, D. Sentman, and E. Wescott, "Imaging of elves, halos, and sprite initiation at 1 ms time resolution," *Journal of Atmospheric and Solar-Terrestrial Physics*, vol. 65, pp. 509-518, 2003.

[26] O. H. Vaughan, Jr., R. Blakeslee, W. L. Boeck, B. Vonnegut, M. Brook, and J. McKune, Jr., "A cloud-to-space lightning as recorded by the space shuttle payload-bay TV cameras," *Monthly Weather Review*, vol. 120, iss. 7, pp. 1459-1461, July 1992.

[27] W. A. Lyons, "Low-light video observations of frequent luminous structures in the stratosphere above thunderstorms," *Monthly Weather Review*, vol. 122, iss. 8, pp. 1940-1946, Aug. 1994.

[28] W. L. Boeck, O. H. Vaughan, Jr., R. J. Blakeslee, B. Vonnegut, M. Brook, and J. McKune, "Observations of lightning in the stratosphere," *Journal of Geophysical Research*, vol. 100, pp. 1465-1475, 1995.

[29] W. L. Boeck, O. H. Vaughan, Jr., R. J. Blakeslee, B. Vonnegut, and M. Brook, "The role of the space shuttle videotapes in the discovery of sprites, jets and elves," *Journal of Atmospheric and Solar-Terrestrial Physics*, vol. 60, no. 7, pp 669-677, May 1998.

[30] C. P. Barrington-Leigh, and U. S. Inan, "Identification of sprites and elves with intensified video and broadband array photometry," *Journal of Geophysical Research*, vol. 106, no. A2, pp. 1741-1750, Feb. 2001.

[31] C. P. Barrington-Leigh and U. S. Inan, "Sprites triggered by negative lighting discharges," *Geophysical Research Letters*, vol. 26, no. 24, pp 3605-3608, Dec 1999.

[32] W. A. Lyons, T. E. Nelson, E. R. Williams, S. A. Cummer, and M. A. Stanley, "Characteristics of sprite-producing positive cloud-to-ground lightning during the

19 July 2000 STEPS mesoscale convective systems," *Monthly Weather Review*, vol. 131, iss. 10, pp. 2417-2427, Oct. 2003.

[33] C. T. R. Wilson, "The electric field of a thundercloud and some of its effects," *Proceedings of the Physical Society of London*, vol. 37, 32D-37D, 1924-1925.

[34] L. C. Hale, "Middle atmosphere electrical structure, dynamics, and coupling," *Advances in Space Research*, vol. 4, issue 4, pp. 175-186, 1984.

[35] M. E. Baginski, "Finite element simulation of the atmosphere's electromagnetic response to charge perturbations associated with lightning," Ph.D. Dissertation, Dept. Elec. Eng., Pennsylvania State Univ., PN, 1987.

[36] V. P. Pasko, "Dynamic Coupling of Quasi-Electrostatic Thundercloud Fields to the Mesosphere and Lower Ionosphere: Sprites and Jets," Ph.D. Dissertation, Dept. Elec. Eng., Stanford Univ., CA, July 1996.

[37] V. P. Pasko, U. S. Inan, and T. F. Bell, "Sprites produced by quasi-electrostatic heating and ionization in the lower ionosphere," *Journal of Geophysical Research*, vol. 102, no. A3, pp. 4529-4561, Mar 1997.

[38] K. Papadopoulos, G. Milikh, A. Gurevich, A. Drobot, and R. Shanny, "Ionization rates for atmospheric and ionospheric breakdown," *Journal of Geophysical Research*, vol. 98, no. A10, pp. 17,593-17,596, Oct. 1993.

[39] V. P. Pasko, U. S. Inan, and T. F. Bell, "Spatial structure of sprites," *Geophysical Research Letters*, vol. 25, no. 12, pp. 2123-2126, June 1998.

[40] C. P. Barrington-Leigh, "Fast photometric imaging of high altitude optical flashes above thunderstorms," Ph.D. Dissertation, Dept. App. Physics, Stanford University, CA, Sept 2000.

[41] Y. N. Taranenko, U. S. Inan, and T. F. Bell, "The interaction with the lower ionosphere of electromagnetic pulses from lightning: Excitation of optical emissions," *Geophysical Research Letters*, vol. 20, no. 23, pp. 2675-2678, Dec. 1993.

[42] R. L. Dowden, and C. J. Rodger, "A vertical-plasma-slab model for determining the lower limit to plasma density in sprite columns from VLF scatter measurements," *IEEE Antennas and Propagation Magazine*, vol. 39, no. 2, Apr. 1997.

[43] R. L Dowden, C. J. Rodger, and D. Nunn, "Minimum sprite plasma density as determined by VLF scattering," *IEEE Antennas and Propagation Magazine*, vol. 43, no. 2, pp. 12-24, Apr. 2001.

[44] M. E. Baginski, L. C. Hale, and J. J. Olivero, "Lighting-related fields in the ionosphere," *Geophysical Research Letters*, vol. 15, no. 8, pp 764-767, Aug 1988.

[45] M. E. Baginski, and D. L. Faircloth, "Peculiarities in the vertical and horizontal electric field signatures in the presence of a sprite," *Proceedings from XXVIIth Triennial General Assembly of the International Union of Radio Science*, Aug 2002.

[46] M. E. Baginski, and D. L. Faircloth, "Finite element modeling of the vertical and horizontal electric field signatures in the presence of a sprite," *Proceedings from 2003 IEEE AP-S International Symposium and USNC National Radio Science Meeting*, The Ohio State Univ., Columbus, Ohio, June 2003.

[47] P. T. Tonev and P. I. Y. Velinov, "Variations of quasi-electrostatic fields and ionosphere potential above lightning discharge at equatorial latitudes," *Advances in Space Research*, vol. 35, iss. 8, pp. 1461-1466, 2005.

[48] M. E. Baginski and G. W. Jarriel Jr., "Characterization of thunderstorm induced Maxwell current densities in the middle atmosphere," *Journal of Electrostatics*, vol. 33, pp. 87-102, 1994.

[49] S. A. Cummer, and M. Füllekrug, "Unusually intense continuing current in lighting produces delayed mesospheric breakdown," *Geophysical Research Letters*, vol. 28, no. 3, pp. 495-498, Feb. 2001.

[50] M. E. Baginski, "Finite element solution of the atmosphere's electromagnetic response to charge perturbations associated with lightning," *Progress in Electromagnetics Research*, vol. 8, pp. 315-364, 1994.

[51] T. F. Bell, V. P. Pasko, and U. S. Inan, "Runaway electrons as a source of Red Sprites in the mesosphere," *Geophysical Research Letters*, vol. 22, no. 16, pp 2127-2130, Aug 1995.

[52] R. H. Picard, U. S. Inan, V. P. Pasko, J. R. Winick, and P. P. Wintersteiner, "Infrared glow above thunderstorms?" *Geophysical Research Letters*, vol. 24, no. 21, pp. 2635-2638, Nov. 1997.

[53] V. P. Pasko, U. S. Inan, and T. F. Bell, "Mesospheric Electric Field Transients due to Tropospheric Lightning Discharges," *Geophysical Research Letters*, vol. 26, no. 9, pp. 1247-1250, May 1999.